The Astrophysical Journal, 995:31 (17pp), 2025 December 10 https://doi.org/10.3847/1538-4357/ae13e3

Spectroscopic Reverberation Mapping for SARM: The Case of Mrk 1048 and Mrk 618

Shivangi Pandey[1,2], Suvendu Rakshit[1], S. Muneer[3], Jincen Jose[1,4], Ashutosh Tomar[1,5], Yan-Rong Li[6], Jian-Min Wang[6], C. S. Stalin[7], Jong-Hak Woo[8], Romain G. Petrov[9], James Leftley[10], Sebastian F. Hönig[10], Amit Kumar Mandal[11], Tushar Ubarhande[1,12], Shu Wang[8], Michael Brotherton[13], and Archana Gupta[2]

[1] Aryabhatta Research Institute of Observational Sciences, Nainital 263001, Uttarakhand, India; Shivangipandey@aries.res.in, suvenduat@gmail.com
[2] Department of Applied Physics/Physics, Mahatma Jyotiba Phule Rohilkhand University, Bareilly 243006, India
[3] Indian Institute of Astrophysics, Bengaluru 560034, India
[4] Center for Basic Sciences, Pt. Ravishankar Shukla University, Raipur, Chhattisgarh 492010, India
[5] Department of Physics, Indian Institute of Technology Roorkee, Roorkee 247667, Uttarakhand, India
[6] Institute of High Energy Physics, Chinese Academy of Sciences, Beijing 100049, People's Republic of China
[7] Indian Institute of Astrophysics, Block II, Koramangala, Bangalore 560034, India
[8] Department of Physics & Astronomy, Seoul National University, Seoul 08826, Republic of Korea
[9] Lagrange Laboratory, Université Côte d'Azur, CNRS, Observatoire de la Côte d'Azur, Nice, France
[10] School of Physics and Astronomy, University of Southampton, Southampton SO17 1BJ, UK
[11] Center for Theoretical Physics of the Polish Academy of Sciences, Al. Lotników 32/46, 02–668 Warsaw, Poland
[12] Department of Applied Optics and Photonics, University of Calcutta, Technology Campus, JD–2, Sector 3, Bidhannagar, Kolkata 700106 West Bengal, India
[13] Department of Physics and Astronomy, University of Wyoming, Laramie, WY 82071, USA

Received 2025 June 20; revised 2025 October 10; accepted 2025 October 11; published 2025 December 3

Abstract

Robust extragalactic distance measurements are crucial for resolving the persistent discrepancy in the value of the Hubble constant (H_0). Active galactic nuclei (AGNs), through their compact and variable broad-line regions, enable the determination of geometric distances when reverberation mapping (RM) is combined with spectroastrometry. We report results from a spectroscopic RM campaign (2022 October–2023 March) targeting two narrow-line Seyfert 1 galaxies, Mrk 1048 and Mrk 618, using the 3.6 m Devasthal Optical Telescope and 2 m Himalayan Chandra Telescope. High-cadence spectrophotometric monitoring was carried out using onboard instruments such as ADFOSC, HFOSC, and TANSPEC, resulting in well-sampled continuum and emission-line light curves. The observed fractional variability ($F_{\rm var}$) ranged from 4% to 14% across the g-band, Hβ, and Hα light curves. The time lags were measured using the interpolated cross-correlation function (ICCF), PyI^{2}CCF, and JAVELIN methods. In the rest frame, the ICCF analysis yields Hβ lags of $10.5^{+2.6}_{-4.2}$ days for Mrk 1048 and $10.2^{+3.4}_{-2.9}$ days for Mrk 618, while the corresponding Hα lags are $18.7^{+5.3}_{-5.4}$ and $14.4^{+4.6}_{-10.5}$ days, respectively. The emission-line widths, measured from the rms spectra using $\sigma_{\rm line}$, give virial black hole mass estimates of $6.3^{+2.0}_{-2.1} \times 10^7\ M_\odot$ for Mrk 1048 and $1.2^{+0.4}_{-0.6} \times 10^7\ M_\odot$ for Mrk 618. These results will serve as a basis for absolute geometric distance calibration when combined with VLTI/GRAVITY spectroastrometric measurements, thereby contributing to the development of AGNs as standardizable cosmological probes.

Unified Astronomy Thesaurus concepts: Reverberation mapping (2019); Active galactic nuclei (16); Black holes (162); Optical telescopes (1174); Distance measure (395)

1. Introduction

Active galactic nuclei (AGNs) are among the most luminous and enduring objects in the Universe, powered by accretion onto supermassive black holes (SMBHs; M. J. Rees 1984) with masses exceeding $10^6\ M_\odot$ (J.-H. Woo & C. M. Urry 2002). Their characteristic broad emission lines and strong continuum variability have long served as vital probes of the central regions of AGNs. A particularly promising geometric approach to studying the broad-line region (BLR) structure (M. Elvis & M. Karovska 2002; S. Rakshit et al. 2015) and measuring AGN distances is the combined use of spectroastrometry and reverberation mapping (SARM) that was first introduced by J.-M. Wang et al. (2020). Spectroastrometry (SA) enables sub-diffraction-limit angular measurements by tracing wavelength-dependent photocenter displacements (S. Rakshit et al. 2015), while reverberation mapping (RM) provides radial BLR sizes based on the time delay between variations in the ionizing continuum and the corresponding response in emission lines. Together, these techniques enable one not only to constrain the geometry and kinematics and measure the black hole masses, but also to estimate the geometric distance independent of the traditional cosmic distance ladder. Applications to a few objects yielded H_0 values consistent with standard cosmology (A. Amorim et al. 2021; Y.-R. Li et al. 2024, 2025). Further theoretical refinements, including modeling of BLR emissivity and responsivity, have improved the accuracy to within ∼10%–30% (Y.-R. Li & J.-M. Wang 2023; Y.-R. Li et al. 2025), although the precision remains constrained by current interferometric capabilities.

RM (J. N. Bahcall et al. 1972; R. D. Blandford et al. 1982; B. M. Peterson 1993), which is a traditional method for studying the central engine of AGNs, uses the time delay between variations in the ionizing continuum (from the accretion disk) and the broad emission lines (from the BLR) to measure the size of the BLR. Assuming the BLR gas is virialized, the SMBH mass can be calculated using the virial

Table 1
Observational Details of Mrk 1048 and Mrk 618

Name	z	D_L (Mpc)	m_V (mag)	$N_{\rm obs}$ Spec.		$\Delta t_{\rm med}$ Spec.		MJD Spec.		Telescopes
				Spec.	Phot.	Spec.	Phot.	Spec.	Phot.	
(1)	(2)	(3)	(4)	(5)	(6)	(7)	(8)	(9)	(10)	(11)
Mrk 1048	0.0426	191.4	14.02	25	125	7	1–3	59856.79–59998.81	59796.33–60001.07	DOT, HCT
Mrk 618	0.0355	154.9	14.10	25	211	7	1–3	59856.87–60014.81	59796.27–60030.60	DOT, HCT

Note. Column (1): object name. Column (2): redshift from NASA/IPAC Extragalactic Database. Column (3): luminosity distance derived from redshift. Column (4): V-band magnitude. Columns (5) and (6): number of observation epochs (spectroscopic and photometric, including ZTF and ASAS-SN). Columns (7) and (8): median sampling interval (spectroscopic and photometric). Columns (9) and (10): duration of observations (spectroscopic and photometric). Column (11): telescopes used.

equation:

$$M_{\rm BH} = \frac{f \times R_{\rm BLR}(\Delta V)^2}{G} \tag{1}$$

where $R_{\rm BLR}$ is the BLR radius (from the time lag), ΔV is the line width (FWHM or $\sigma_{\rm line}$), and f is the virial factor inferred from BLR geometry and inclination. RM has been applied to over a hundred AGNs, successfully calibrating the $R_{\rm BLR}$–L_{5100} relation (S. Kaspi et al. 2000; M. C. Bentz et al. 2013; H. Cho et al. 2023; J.-H. Woo et al. 2024; C. Sobrino Figaredo et al. 2025), and yielding insights into black hole mass scaling relations, AGN structure, and accretion physics (e.g., Y. Shen et al. 2011, 2024; P. Du et al. 2015, 2016; L. Pei et al. 2017; C. J. Grier et al. 2017; S. Rakshit et al. 2019; E. M. Cackett et al. 2021; V. U et al. 2022; H. Cho et al. 2023; S. Wang & J.-H. Woo 2024; J.-H. Woo et al. 2024; C. Sobrino Figaredo et al. 2025). The velocity-resolved delay map and dynamical modeling of RM data showed evidence for Keplerian rotation of the BLR clouds and a disk-like BLR in many AGNs (e.g., A. Pancoast et al. 2014; Y.-R. Li et al. 2018; S. Wang et al. 2025). However, these are limited by the requirements of better and higher-cadence data.

Despite its success, RM is fundamentally limited by its inability to resolve full spatial structures, as it probes only line-of-sight velocities. This constraint has been significantly alleviated by advances in optical/IR interferometry. In particular, the GRAVITY instrument on the VLTI has spatially resolved BLRs in nearby AGNs with $\sim$10 μas precision, observing sources such as 3C 273 and NGC 3783 (Gravity Collaboration et al. 2018, 2020; A. Amorim et al. 2021). GRAVITY has also revealed a strong correlation between hot dust sizes and RM-based BLR radii, offering an alternative path for SMBH mass estimation with fewer observational demands (GRAVITY Collaboration et al. 2024). Combined with RM, this enables a complementary spatial–temporal view of BLR geometry.

To fully exploit SARM for distance measurements and SMBH mass estimation, high-quality RM data remain essential. While GRAVITY/VLTI provides angular sizes for nearby AGNs, accurate linear sizes for BLRs from RM are needed to derive angular diameter distances. This requires long-term, high-cadence spectroscopy of AGNs with strong, variable broad lines. Motivated by this, we initiated an RM campaign targeting AGNs observable with GRAVITY/VLTI, aiming to measure time lags between the ionizing continuum and broad-line variations. These lags yield estimates of the BLR radii and virial mass for future SARM studies. This paper presents the campaign's initial results, variability analysis, lag measurements, and black hole mass estimates. Section 2 details the target selection and observations; Section 3 describes data processing and light-curve analysis; Section 4 presents lag measurements via the interpolated cross-correlation function (ICCF) and JAVELIN; Section 5 describes the effect of detrending on the light curve and results; Section 6 covers methods of mass estimation; Section 7 offers comparisons and implications; and Section 8 summarizes our findings.

2. Target Selection and Observations

To assemble a sample suitable for SARM observations from both hemispheres, we began with the catalog of J.-M. Wang et al. (2020), which lists 30 low-redshift AGNs ($z < 0.08$) with $K < 11.5$ and expected BLR angular sizes $\gtrsim$20 μas. These characteristics make them promising candidates for distance measurements using strong Brackett γ or Paschen α emission lines accessible to GRAVITY. Among these 30 AGNs, only seven have declinations higher than $-15°$ and K-band magnitudes brighter than 11, rendering them accessible to ground-based observatories in both hemispheres. Initially, we planned to monitor all seven sources using the 3.6 m Devasthal Optical Telescope (DOT; B. Kumar et al. 2018), ARIES, Nainital and the 2 m Himalayan Chandra Telescope (HCT) at the Indian Astronomical Observatory (IAO), Hanle, India, as part of this campaign. Over 5–6 months, i.e., 2022 October to 2023 March, four AGNs were successfully observed. However, data quality was affected by external factors such as seasonal gaps, weather conditions, variability constraints, and cadence issues. Ultimately, only two out of four sources, Mrk 1048 and Mrk 618, exhibited well-sampled light curves with better cadence spectroscopic monitoring and strong correlation properties. Table 1 depicts the different properties for Mrk 1048 and Mrk 618, including redshift, luminosity distance, magnitude in the V band, corrected for extinction, the total number of epochs of spectroscopic and photometric observations, the cadence in both, the period of observations, and telescopes.

Weekly cadence spectroscopic and photometric observations of both sources were carried out using optical and near-infrared spectrographs mounted on the 3.6 m DOT and the 2 m HCT. Optical spectrophotometric data with DOT were obtained using the ARIES Devasthal Faint Object Spectrograph and Camera (ADFOSC; A. Omar et al. 2019). ADFOSC features a 4K × 4K deep-depletion CCD camera, yielding a pixel scale of $0\farcs2$ pixel^{-1} with 2×2 binning (D. Panchal et al. 2023). However, due to technical reasons (limited ports to mount the instrument at DOT), the optical spectrograph ADFOSC, which covers both the Hβ and Hα

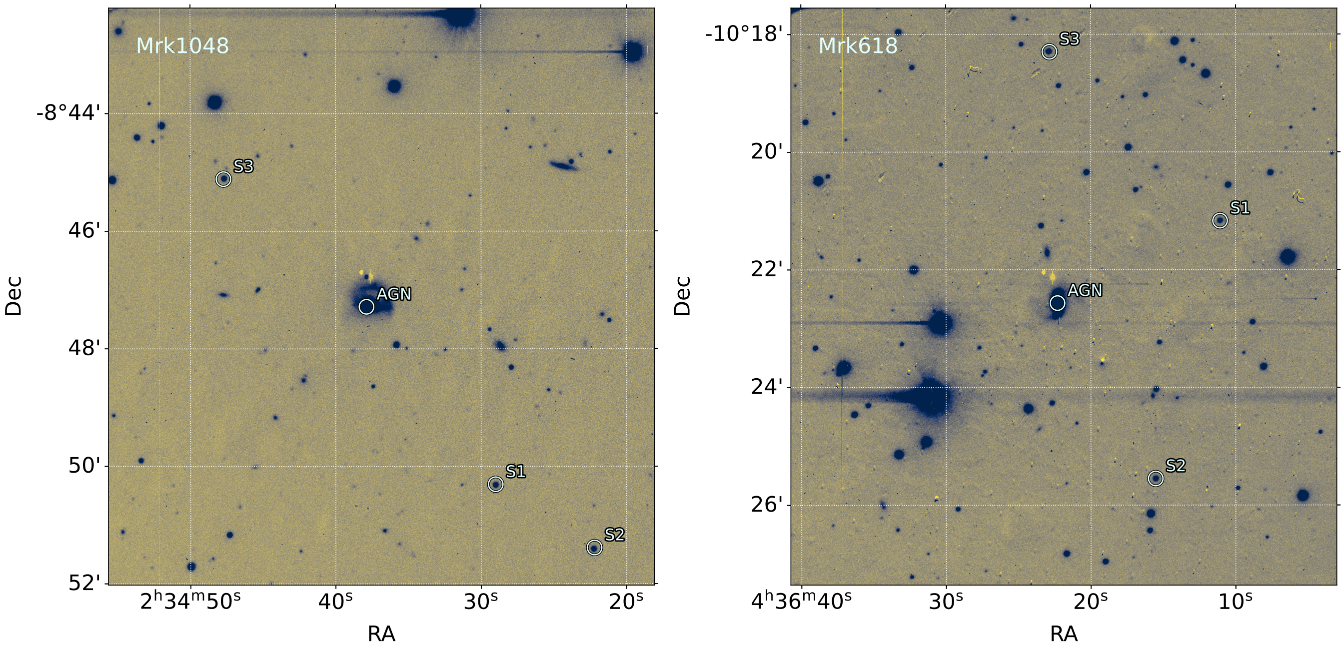

Figure 1. *V*-band image of Mrk 1048 and Mrk 618 observed from the HFOSC/HCT with a field of view of $10' \times 10'$. The sources are marked, and the nearby comparison stars are shown.

lines, is available for ∼2 months in each observation cycle. Therefore, we have also used the TIFR-ARIES Near Infrared Spectrometer (TANSPEC; S. Sharma et al. 2022) (mounted at DOT alternatively with ADFOSC), which covers the optical Hα line (0.6–2.2 μm) along with other infrared emission lines. TANSPEC is equipped with two Teledyne HgCdTe Astronomical Wide Area Infrared Imager (HAWAII) detectors: an H1RG (1024×1024 pixels) for imaging and slit viewing, and an H2RG (2048×2048 pixels) for spectroscopy. The instrument offers a 1×1 arcmin^2 field of view (FOV) and covers a wavelength range of 0.55–2.5 μm, split into 10 spectral orders.

Optical observations with the HCT utilized the Himalayan Faint Object Spectrograph Camera (HFOSC),[14] a versatile instrument designed for low- and medium-resolution grism spectroscopy. The detector comprises a SITe ST-002 2K × 4K pixel CCD, with the central 2K × 2K region used for imaging. This setup provides an FOV of approximately $10' \times 10'$ and a pixel scale of $0\overset{\prime\prime}{.}296$ pixel^{-1}.

2.1. Photometry

Photometric observations were conducted using broadband filters, specifically the Sloan Digital Sky Survey (SDSS) *r* band (623 nm) from ADFOSC, the *V* band (550 nm) from HFOSC, and the *R* band (612 nm) from TANSPEC. For each target, three broadband photometric frames were acquired with exposure times ranging from 30 to 60 s, immediately preceding the spectroscopic observations. Figure 1 presents the *V*-band images of Mrk 1048 and Mrk 618, with the central AGN marked. Images obtained from each observation night were initially aligned using the Astroalign Python package (M. Beroiz et al. 2020). The preprocessing of photometric frames followed standard procedures, including bias subtraction, flat-field correction, and cosmic-ray removal. Aperture photometry was carried out using SEP, a Python-based wrapper for the Source Extractor package (K. Barbary 2016). Differential photometry was performed by selecting 3–5 nearby reference stars, as shown in Figure 1. The photometric aperture was set to 2.5 times the average FWHM of the selected comparison stars, where the FWHM was determined by fitting a Gaussian profile to the data. The local sky background was estimated within an annular region extending from four to five times the FWHM. The differential magnitude of the source was then calculated relative to the comparison stars in the same FOV. Finally, a photometric zero-point was applied to convert instrumental magnitudes into calibrated broadband magnitudes.

In addition to our observations, we incorporated archival *g*-band photometric data from two public time-domain surveys: the All-Sky Automated Survey for Supernovae (ASAS-SN; C. S. Kochanek et al. 2017) and the Zwicky Transient Facility (ZTF; M. J. Graham et al. 2019). To ensure photometric quality, we selected only high-quality measurements by applying a flag condition of bad catflags ask = 0, which excludes data points marked with any known issues such as saturation, blending, or poor centroiding. This effectively removes outliers and spurious detections from the ZTF light curves. These datasets span the period from 2022 May to 2023 March. Given the higher cadence of the ASAS-SN *g*-band data (centered at 4747 Å), we intercalibrated all photometric measurements from other bands to the ASAS-SN scale using the `PyCALI` software (Y.-R. Li et al. 2014). This intercalibration significantly enhanced the temporal sampling of the light curves, as summarized in Table 1. For the subsequent analysis, we adopt the intercalibrated *g*-band light curve as the primary continuum-driving signal.

2.2. Spectroscopy

Spectroscopic observations were conducted using three instruments: ADFOSC and TANSPEC mounted on the 3.6 m DOT, and HFOSC on the 2 m HCT, each configured to obtain high-quality spectral data. Below, we detail the setup and reduction procedures used for each instrument.

---

[14] https://www.iiap.res.in/centers/iao/facilities/hct/

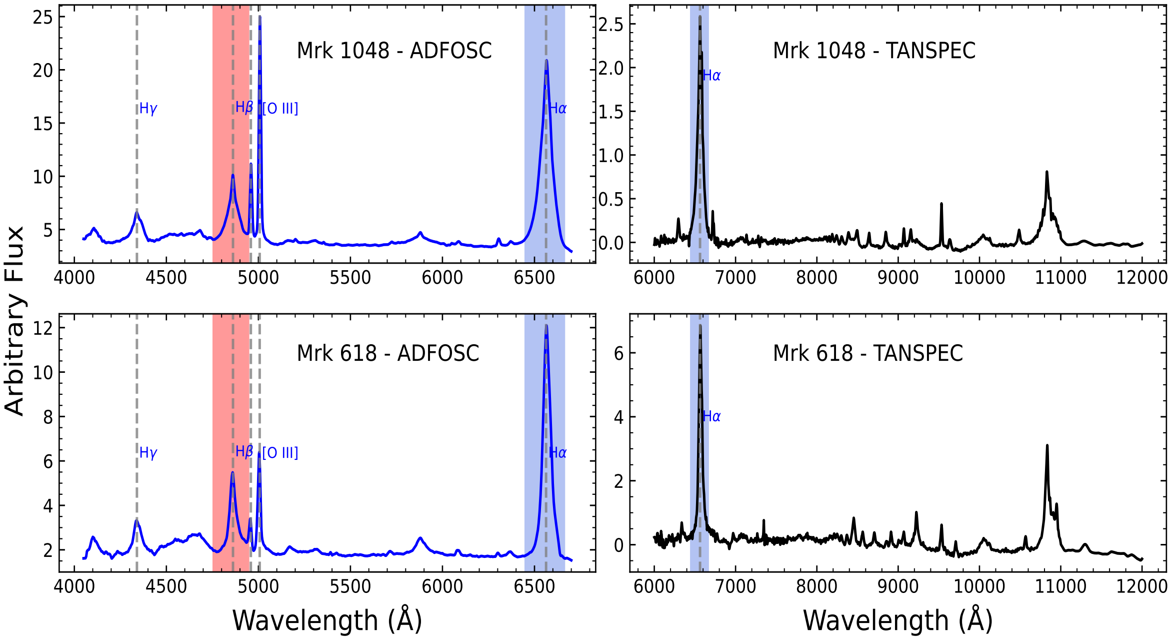

Figure 2. The composite spectra from ADFOSC (left) and TANSPEC (right) of Mrk 1048 (top) and Mrk 618 (bottom). The emission-line regions, such as Hγ, Hβ, and Hα, with narrow emission lines [O III] are highlighted.

(1) ADFOSC (mounted on the 3.6 m DOT) spectroscopic observations were performed using a 1$''$.2 wide and 8$''$ long slit in combination with a 132R-600 grooves mm^{-1} grism, covering the wavelength range 3500–7000 Å, and centered at 4880 Å. Each spectroscopic frame had an exposure time of 600 s. Bias and flat-field frames were also acquired throughout the night for standard calibration. Seeing conditions during the observations ranged between 0$''$.5 and 1$''$.5. The instrumental resolution was determined to be 7 Å (corresponding to 312 km s^{-1}), measured by modeling the emission lines in a combined Hg–Ar–Ne arc lamp frame taken with the same configuration as the science exposures.

(2) HFOSC (mounted on the 2 m HCT) spectroscopic data were obtained using Grism 7, which provides a spectral resolution of $R = \lambda/\Delta\lambda \sim 1320$ and covers a wavelength range of 3800–6840 Å. Observations employed a 1$''$.15 wide and 11$'$ long slit. Wavelength calibration was carried out using Fe–Ar and Fe–Ne hollow cathode lamps, taken immediately before and after the science frames. The observations were conducted under good photometric conditions, with an average FWHM seeing of approximately 1$''$.6. Bias and flat-field calibration frames were collected at the beginning and end of each night. The resulting spectral resolution achieved was 8 Å.

Spectroscopic data reduction was performed using IRAF (D. Tody 1986, 1993; National Optical Astronomy Observatories 1999), following standard procedures including bias subtraction, flat-fielding, and cosmic-ray removal using the L.A. Cosmic algorithm (P. G. van Dokkum 2001). Flat-field correction was applied using a tungsten LED lamp for ADFOSC and a halogen lamp for HFOSC, with both lamps normalized before division by the science frames. Spectral extraction was carried out using the "apall" task in IRAF, with an aperture size of 7$''$–8$''$ set for both the target source and comparison stars. Wavelength calibration for ADFOSC spectra was performed using Hg–Ar and neon arc lamps, whereas Fe–Ar and Fe–Ne lamps were used for HFOSC data. All calibration lamps were observed in the same instrumental configuration as the respective science exposures. For ADFOSC, the calibration lamp frames were combined using the "imcombine" task in IRAF. The resulting combined calibration spectrum was then used to derive the wavelength solution, which was subsequently applied to both the science and reference stellar spectra. Flux calibration was achieved using a spectrophotometric standard star, from which a sensitivity function was derived and applied. Figure 2 displays the mean spectrum obtained from all ADFOSC observations, with prominent emission-line regions indicated. The upper and lower left panels correspond to Mrk 1048 and Mrk 618, respectively.

(3) The TANSPEC (mounted on the 3.6 m DOT) spectrograph has two operational modes, capturing spectral data on a 2K × 2K H2RG array. We have carried out spectroscopic observations in the cross-dispersed (XD) mode, which uses a combination of a grating and two prisms that are employed to pack all spectral orders onto the H2RG detector, achieving a resolution of $R \sim 1500$ for a 1$''$ slit width. Standard observational procedures were followed: each target was nodded along the slit at two positions, with multiple exposures taken at each nod to enhance the signal-to-noise ratio. Exposure times were limited to three minutes per frame to facilitate effective cancellation of telluric emission lines through frame differencing at alternating nod positions. Telluric correction was performed using a nearby A0V-type standard star. Additionally, argon and neon arc lamps were used for wavelength calibration, and tungsten lamps were employed for flat-fielding. Calibration frames were acquired for each target to ensure accurate and precise spectral calibration. Data reduction was carried out using the `pyTANSPEC` pipeline (S. Ghosh et al. 2023),[15] a dedicated tool designed for reducing TANSPEC XD-mode spectra. The extracted spectra were corrected for telluric absorption features

---

[15] https://github.com/astrosupriyo/pyTANSPEC

and subsequently normalized. Continuum-normalized spectra from different spectral orders were combined to construct a final composite spectrum for each source. Flux calibration of the TANSPEC spectra was performed using a telluric standard star and photometric observations taken around the same time, and the spectral slope was adjusted based on data from the HCT or ADFOSC instrument on DOT. A nearby epoch spectrum from HCT or DOT was used to measure the slope of the source continuum, which was then applied to the wavelength-calibrated TANSPEC spectrum. After this correction, the spectrum was rescaled to match the corresponding photometric flux, ensuring consistency between the spectral and photometric data. Figure 2 shows the composite mean spectra of Mrk 1048 and Mrk 618 in the upper and lower right panels, respectively. The Hα emission line and several Paschen series lines are prominently visible. However, in Figure 2 only a small portion of the spectrum is visible to highlight the Hα emission line. The spectra are comparatively noisier due to residual telluric features and gaps in atmospheric transmission.

3. Analysis

3.1. Spectral Decomposition

Accurate RM measurements require precise estimation of the intrinsic variability of AGNs, necessitating correction for extrinsic factors such as changes in observing conditions. Failure to account for such effects can result in the misattribution of variability to intrinsic AGN emission. To mitigate this, we employed the `mapspec` Python package[16] (M. M. Fausnaugh 2017), which implements a Bayesian framework based on the method of E. van Groningen & I. Wanders (1992). It applies an empirical template to correct time-series spectra for variations in wavelength calibration, attenuation, and spectral resolution. For spectral calibration, the [O III] λ5007 emission line was used as a nonvariable reference feature to rescale spectra and correct for redshifts at each epoch for both sources. The [O III] extraction windows were defined as [4984, 5025] Å for Mrk 1048 and [4990, 5027] Å for Mrk 618, to account for source-specific differences in line width. The adjacent continuum windows were set as [4980, 4990] Å and [5027, 5037] Å for Mrk 1048, and [4974, 4984] Å and [5025, 5035] Å for Mrk 618.

The `mapspec` package standardized the [O III] profiles across all epochs by correcting for wavelength shifts, flux scaling, and line broadening using a Gauss–Hermite kernel (M. M. Fausnaugh et al. 2017). The reference epoch was selected based on the spectrum exhibiting the broadest [O III] profile and using HCT spectral [O III] flux having a comparatively large number of data points, typically corresponding to data acquired under poor seeing conditions or affected by slit losses. Calibration uncertainties were measured using a Markov Chain Monte Carlo (MCMC) approach. The resulting flux scaling uncertainties were combined in quadrature with the measurement errors of the Hβ flux, ensuring accurate propagation of calibration errors into the final light curve. The publicly available multicomponent spectral fitting code PyQSOFit, developed by H. Guo et al. (2018), was employed for spectral decomposition and line fitting. A comprehensive description of the code and its applications is given by H. Guo et al. (2019), Y. Shen et al. (2019), and S. Rakshit et al. (2020). Each AGN spectrum was first corrected for Galactic extinction using the reddening map of D. J. Schlegel et al. (1998) and the Milky Way extinction law of E. L. Fitzpatrick (1999), adopting $R_V = 3.1$. The spectra were then de-redshifted using the redshifts listed in Table 1. The underlying continuum was modeled with a power-law fit over selected line-free regions of the spectrum, specifically [4200, 4260], [4435, 4640], [5100, 5535], [6005, 6035], and [6110, 6250] Å. Additionally, Fe II emission was modeled using templates from T. A. Boroson & R. F. Green (1992). The signal-to-noise ratio (S/N) in continuum regions around 5100 Å was typically in the range 20–30 for both sources. Following continuum subtraction, detailed multi-Gaussian modeling was performed in the Hβ and Hα regions, as illustrated in Figure 3. The narrow components of Hβ, [O III] λ5007, [O III] λ4959, Hα, [N II] λ6549, and [N II] λ6585 were each modeled using a single Gaussian, with their velocities and velocity offsets tied together to ensure consistency. The broad components of Hβ and Hα were modeled using two Gaussians to account for the peak and extended wings. The best-fitting models were determined through χ^2 minimization. From the resulting models, we extracted emission-line fluxes and line widths. The continuum luminosities at 5100 Å were measured within a 40 Å window centered on the line 5100 Å (±20 Å on either side). For TANSPEC spectra, the continuum was modeled using a power-law fit over selected line-free regions: [6502, 6645], [10736, 11005], [12700, 13000], [14765, 15755], and [19017, 19524] Å. After subtracting the fitted continuum, spectral decomposition was performed in the Hα region, using a single-Gaussian profile fit within the wavelength range 6400–6670 Å. The integrated flux of the Hα line was then calculated by integrating the best-fitting Gaussian model.

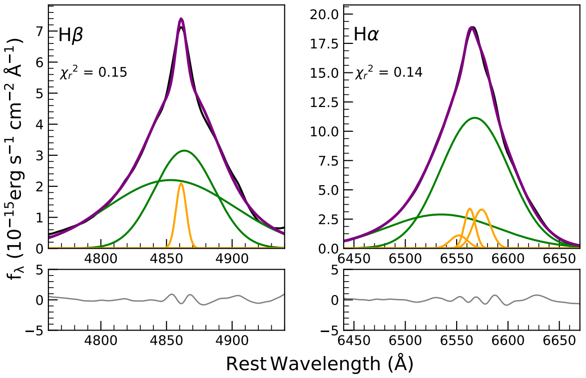

Figure 3. The Hβ (left) and Hα (right) emission-line plots are shown along with their residuals after fitting for Mrk 1048. The broad component fitting with a double Gaussian is in green, whereas the narrow component fitting is shown in orange. The total line model is overplotted on the original continuum-subtracted spectrum. The Hα emission-line fittings have decomposed the [N II] λ6549, [N II] λ6585, and narrow Hα components.

3.2. Light Curve and Variability

For data obtained from ADFOSC and HFOSC, the emission-line fluxes for Hβ and Hα were measured by integrating the area under the broad components modeled using best-fitting Gaussians from PyQSOFit, centered at 4861 Å and 6564 Å. The rest-frame wavelength ranges used for integration were [4780, 4940] Å for Hβ and [6450, 6680] Å

---

[16] https://github.com/mmfausnaugh/mapspec/

for Hα, with these regions consistently applied to both sources. However, the line widths and flux strengths differed significantly between Mrk 1048 and Mrk 618, reflecting source-specific kinematics and variability. In addition to the Hα fluxes derived from TANSPEC (using single-Gaussian fitting), we employed `PyCALI` once again to intercalibrate the Hα light curves obtained with ADFOSC and HFOSC against those from TANSPEC. This step was essential to correct for noticeable flux offsets present in the TANSPEC spectra. However, since the TANSPEC dataset contains only a limited number of observations (5 or 6 data points), the use of `PyCALI` introduces relatively larger uncertainties, which in turn affect the final flux calibration. To mitigate this issue, we smoothed the Hα light curve by applying a five-point running average. The final intercalibrated Hα and Hβ emission-line light curves were then used for lag measurements for the photometric g-band continuum light curve. Understanding short-term intrinsic variability is crucial for determining accurate lags. The final light curves are shown in Figure 4. The upper panel displays the g-band photometric continuum, with marked data points from different telescopes. The middle panel presents the Hβ emission-line light curve from ADFOSC and HFOSC observations, while the bottom panel shows the intercalibrated Hα emission-line light curve, including data points from TANSPEC. For Mrk 618, we have added the Hβ flux points from Season 4 of T. E. Zastrocky et al. (2024) to our obtained Hβ light curve for better cadence and correlation analysis.

Typical light-curve parameters—the fractional variability amplitude ($F_{\rm var}$), the maximum-to-minimum flux ratio ($R_{\rm max}$), and the median flux—are summarized in Table 2. The fractional variability amplitude was calculated using the equation (P. M. Rodriguez-Pascual et al. 1997)

$$F_{\rm var} = \frac{\sqrt{\sigma^2 - \langle\sigma_{\rm err}^2\rangle}}{\langle f\rangle} \tag{2}$$

where σ^2 is the variance of the light curve, $\langle\sigma_{\rm err}^2\rangle$ is the mean square measurement uncertainty, and $\langle f\rangle$ is the mean flux.

Mrk 1048. The properties of the light curves for Mrk 1048 are listed in the first three rows of Table 2. $F_{\rm var}$ for the photometric g-band continuum is approximately 7.30%. The variability amplitudes for the Hβ and Hα emission lines are higher, at 10.3% and 6.75%, respectively. As expected, the median flux of the Hα line exceeds that of Hβ, reflecting the differences in intrinsic line strength between them (D. E. Osterbrock & G. J. Ferland 2006; H. Netzer 2013). The typical Hα/Hβ flux ratio is around 3, and our results are broadly consistent with this value. Median flux values are reported in magnitudes for the g-band and in units of 10^{-13} erg s^{-1} cm^{-2} Å^{-1} for the emission lines. The maximum-to-minimum flux ratios ($R_{\rm max}$) are 1.42, 1.50, and 1.27 for the g band, Hβ, and Hα, respectively.

Mrk 618. The light-curve parameters for Mrk 618 are presented in the last three rows of Table 2. The g-band continuum exhibits a relatively lower $F_{\rm var}$ of approximately 4.20%. The emission lines show moderately higher variability, with $F_{\rm var}$ values of 7.68% for Hβ and 13.91% for Hα. The greater scatter may partly influence the higher variability amplitude observed for Hα in the TANSPEC data points and host-galaxy dilution. Corresponding $R_{\rm max}$ and median flux values are also listed. As is evident from Figure 4, the emission-line light curves for Mrk 618 also show more pronounced variability than the photometric continuum. Additionally, the line strength of Hα is ≈3 times more prominent than that of Hβ, similar to the median flux of Mrk 1048.

4. Time Lag Measurement

4.1. ICCF and JAVELIN

To measure the time between the continuum variations and the Hβ and Hα emission-line responses, we employed two widely adopted techniques: the ICCF[17] (C. M. Gaskell & L. S. Sparke 1986; B. M. Peterson et al. 1998) and the model-based code JAVELIN[18] (Y. Zu et al. 2011, 2013). Both methods have been extensively validated in the context of RM studies (see B. M. Peterson et al. 1998, 2004; M. C. Bentz et al. 2014; A. J. Barth et al. 2015; J.-H. Woo et al. 2024) and typically produce broadly consistent results (R. Edelson et al. 2019). The ICCF approach involves computing the cross-correlation function between the continuum and emission-line light curves to identify the degree of correlation and the corresponding time lag. We explored a lag search range from −20 to +100 days, guided by previously reported lags for both sources (typically within ∼30 days; V. U et al. 2022; T. E. Zastrocky et al. 2024) and our total monitoring baseline. Following the approach discussed by J.-H. Woo et al. (2024), where it is emphasized that too wide a lag window may introduce spurious secondary peaks or dilute the correlation strength due to noise and sparse sampling, we tested narrower windows around the expected lag range. We found that the posterior lag distributions consistently peaked at the same locations, though with slightly lower correlation coefficients ($r_{\rm max}$) when using wider windows. When we refined the lag search window to −10 to +50 days for Mrk 1048 and Mrk 618, the primary ICCF peak remained prominent and $r_{\rm max}$ increased, suggesting improved sensitivity and reduced contamination from false correlations. Moreover, we do not have to deal with seasonal gaps as our monitoring period is roughly 5 months. To account for irregular time sampling, the ICCF method interpolates one light curve while holding the other fixed. Then, it averages the results of both configurations to construct the final cross-correlation function.

We used the flux randomization/random subset sampling Monte Carlo technique (B. M. Peterson et al. 1998, 2004) to quantify the uncertainty in lag measurements. This involves generating multiple realizations of the light curves by resampling and perturbing the data and computing the centroid lag ($\tau_{\rm cent}$) from the portion of the CCF above 80% of the peak $r_{\rm max}$, also highlighted in Figure 4. The median of the resulting $\tau_{\rm cent}$ distribution is adopted as the best-measure lag. The derived lag values for both methods are summarized in Table 3.

JAVELIN, developed by Y. Zu et al. (2011, 2013), models AGN continuum variability using a damped random walk (DRW; B. C. Kelly et al. 2009, 2014) process and derives emission-line light curves by convolving the modeled continuum with a transfer function, typically a top-hat function. Uncertainties on the lag and other parameters are measured using an MCMC approach, which provides statistical confidence intervals for the best-fit values. JAVELIN

---

[17] https://bitbucket.org/cgrier/python_ccf_code/src/master/

[18] https://github.com/nye17/JAVELIN

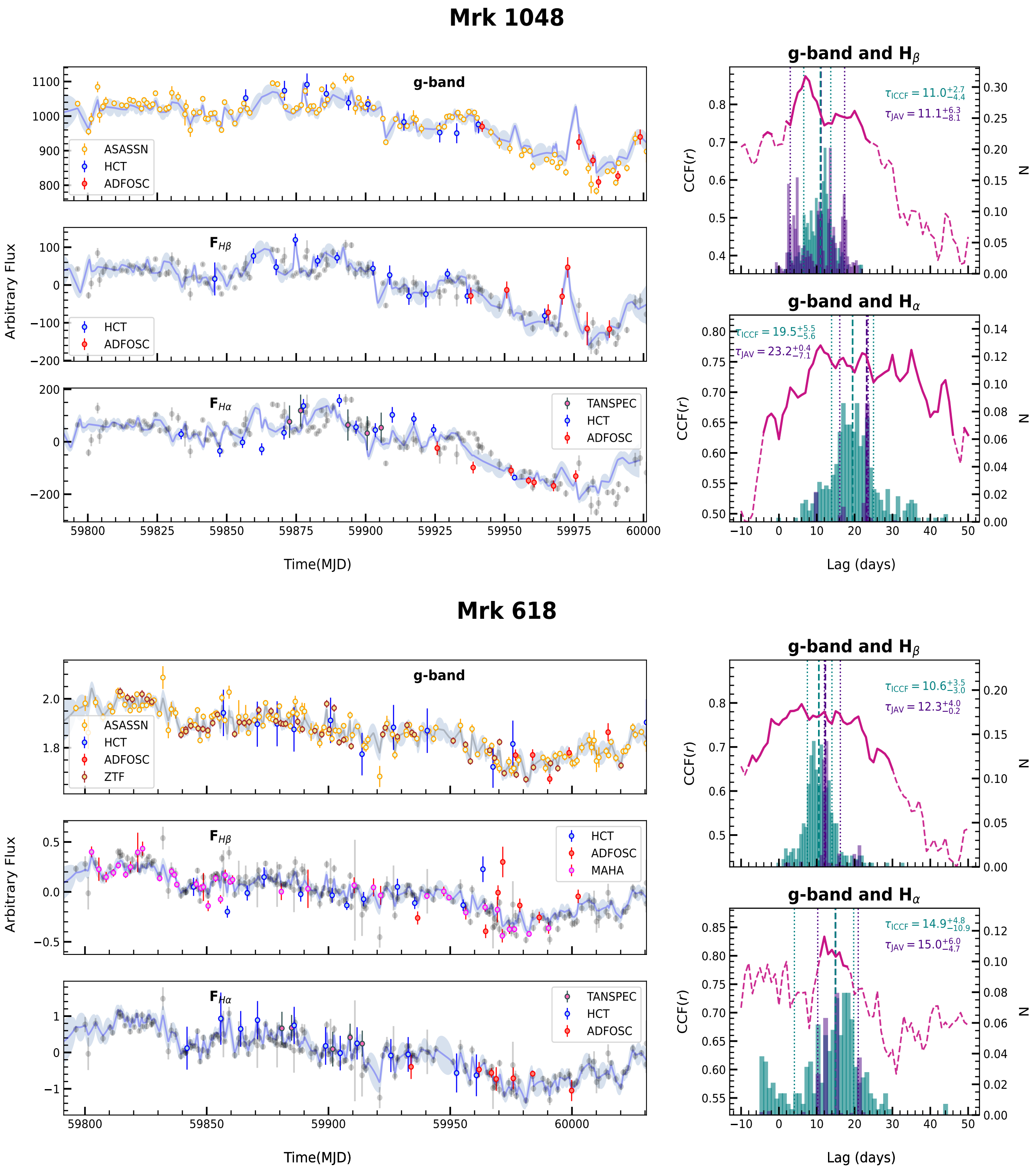

Figure 4. Light curve plots for Mrk 1048 and Mrk 618. The upper panel shows a photometric g-band continuum with labeled data points from each telescope. The middle left and lower left panels display Hβ and Hα emission-line fluxes in arbitrary units, with g-band continuum overlaid. These are mean-subtracted light curves and are matched by normalizing the g-band continuum light curve and shifting the emission-line light curves to the final adopted lag values mentioned in Table 3. The JAVELIN modeling for each light curve is shown in steel blue. For the Hα light curve, we have smoothed it with five consecutive points using the running average method. The upper and lower right panels show the lag histograms from ICCF (teal) and JAVELIN (violet). These plots display the CCF value $r_{\rm value}$ on the left (pink) and the probability density (N) of the histograms on the right. The darker pink region of the $r_{\rm value}$ curve depicts 80% of the centroid peak that is used to calculate the final ICCF lag. The dashed lines indicate the lags with 16th and 84th percentiles of the lag probability density.

simultaneously models both continuum and emission-line light curves. The DRW model has been shown to reproduce AGN variability on both short and long timescales across multiple bands, with some exceptions (e.g., I. M. McHardy et al. 2006; R. F. Mushotzky et al. 2011). Compared to ICCF, JAVELIN often produces tighter constraints on lag measures (e.g., R. Edelson et al. 2019; Z. Yu et al. 2020). Table 3 presents the lag results.

Mrk 1048. The ICCF analysis yields a lag of $11.0^{+2.7}_{-4.4}$ days with a well-defined peak and a maximum cross-correlation coefficient ($r_{\rm max}$) of 0.88, whereas JAVELIN yields $11.1^{+6.3}_{-8.1}$ days between the g band and Hβ, being consistent within the errors. For the g band versus Hα, ICCF and JAVELIN give lag values of $19.5^{+5.5}_{-5.6}$ and $23.2^{+0.4}_{-7.1}$ days, respectively, with $r_{\rm max} > 0.75$ for the ICCF. The Hβ lags were comparatively shorter than the Hα lag values from each method, hinting at the BLR stratification (M. C. Bentz et al. 2010). The lag distributions are visualized in Figure 4 (right panels). For the g band versus Hβ, the ICCF and JAVELIN lag distributions are confined within 0–25 days with a very sharp peak near measured lag

Table 2
Variability Statistics

Source	Parameter	g band	Hβ	Hα
Mrk 1048	$F_{\rm var}(\%)$	7.30 ± 0.47	10.30 ± 0.17	6.75 ± 0.14
	$R_{\rm max}$	1.42 ± 0.03	1.50 ± 0.04	1.27 ± 0.03
	Median	14.19 ± 0.01	4.15 ± 0.12	13.6 ± 2.50
Mrk 618	$F_{\rm var}(\%)$	4.20 ± 0.24	7.68 ± 0.83	13.91 ± 2.00
	$R_{\rm max}$	1.25 ± 0.03	1.42 ± 0.06	1.65 ± 0.01
	Median	14.37 ± 0.05	2.50 ± 0.34	4.12 ± 0.14

Notes. Variability statistics ($F_{\rm var}$), the maximum-to-minimum flux ratio ($R_{\rm max}$), and median values with their respective errors for the g band, Hβ, and Hα in Mrk 1048 and Mrk 618. The median flux is in magnitudes for the g band, and in units of 10^{-13} erg s^{-1} cm^{-2} Å^{-1} for Hβ and Hα emission lines.

Table 3
Measured Time Delays (Lags) for Mrk 1048 and Mrk 618 Using ICCF, JAVELIN, and PyI^{2}CCF Methods

Source	Light Curve	ICCF		JAVELIN	PyI^{2}CCF	
		Lag (days)	$r_{\rm max}$	Lag (days)	Lag (days)	p-value
(1)	(2)	(3)	(4)	(5)	(6)	(7)
Mrk 1048	g band versus Hβ	$11.0^{+2.7}_{-4.4}$	0.9	$11.1^{+6.3}_{-8.1}$	$11.4^{+3.1}_{-4.1}$	0.09
	g band versus Hα	$19.5^{+5.5}_{-5.6}$	0.7	$23.2^{+0.4}_{-7.1}$	$20.1^{+6.7}_{-6.1}$	0.16
Mrk 618	g band versus Hβ	$10.6^{+3.5}_{-3.0}$	0.7	$12.3^{+4.0}_{-0.2}$	$12.0^{+7.5}_{-7.0}$	0.06
	g band versus Hα	$14.9^{+4.8}_{-10.9}$	0.8	$15.0^{+6.0}_{-4.7}$	$14.0^{+4.4}_{-8.8}$	0.04

Notes. Lags are in the observer frame for g band versus Hβ and Hα emission-line light curves. Columns: (1) source; (2) light curve chosen to calculate the lag; (3) ICCF centroid lag; (4) cross-correlation coefficient $r_{\rm max}$; (5) JAVELIN lag; (6) PyI^{2}CCF lag; (7) PyI^{2}CCF null-hypothesis value (p). The lag search range for both sources, Mrk 1048 and Mrk 618, is between −10 and 50 days.

values. In contrast, for the g band versus Hα, the JAVELIN posterior distribution is narrower than the ICCF lag distribution with three sharp peaks, which is widely spread until 25 days. The lag results for Hβ are broadly consistent with those reported by V. U et al. (2022) as part of the LAMP 2016 campaign, where a rest-frame lag of $\tau_{\rm cent} = 9.0^{+9.4}_{-7.4}$ days was measured with $r_{\rm max}$ appears more likely as a flat top. Our monitoring over a longer duration yields a more sharply defined lag with a higher $r_{\rm max} = 0.88$, improving upon the earlier constraints.

Mrk 618. The lag measurements from ICCF and JAVELIN are $10.6^{+3.5}_{-3.0}$ and $12.3^{+4.0}_{-0.2}$ days, respectively, with a maximum correlation coefficient ($r_{\rm max}$) of approximately 0.72, as reported in Table 3. The measured lag for the g band versus Hα light curves is consistent and similar to that for Hβ within error, with $14.9^{+4.8}_{-10.9}$ days ($r_{\rm max} = 0.81$) obtained via ICCF and $15.0^{+6.0}_{-4.7}$ days via JAVELIN. The lag distributions for these pairs, shown in the upper and lower right panels of the second row in Figure 4, reveal stronger confined peaks for Hβ and Hα. Uncertainties for both methods were derived from the entire probability of the lag distributions. The lag results are very similar to those reported by T. E. Zastrocky et al. (2024, hereafter referred to as the Monitoring AGNs with Hβ Asymmetry (MAHA) survey). They provided a range of lag values obtained over four seasons, and our results for Hβ are in agreement with their lag value measured in the fourth season.

4.2. Simulations

To assess the robustness of our measured lags and determine whether the observed time sampling is adequate for reliable lag detection, we performed extensive light-curve simulations. For each source (Mrk 1048 and Mrk 618), we generated mock continuum light curves based on the DRW model, with parameters tuned to match the variability amplitude and timescale of the observed g-band continuum. Importantly, the simulated light curves were constructed with the same temporal sampling and data gaps as the real observations, thereby preserving realistic observational conditions. The emission-line light curves for Hβ and Hα were then synthesized by shifting, smoothing, and scaling the mock continuum light curves using the observed lag values derived from our ICCF analysis (see Table 3). We applied both ICCF and JAVELIN time-series analysis methods to each realization in order to recover the input lag. This process was repeated for 1000 independent simulations for each emission line and each source.

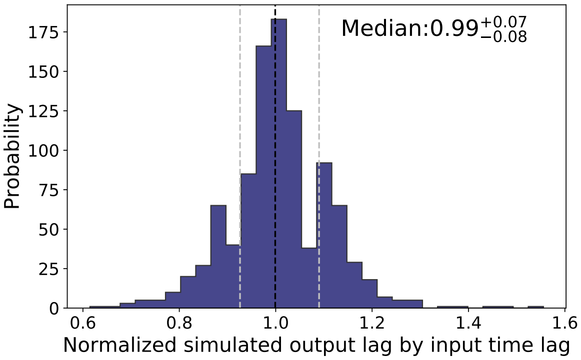

Figure 5. We simulated light curves for the g-band continuum and the Hβ and Hα emission lines with 1000 independent realizations each. The figure shows the probability distribution of the ratio between the recovered lag and the input ICCF lag (11 days) for the case of the g band versus Hβ for Mrk 1048 with the ICCF method. The quoted median of the distribution is close to unity, indicating that the observed sampling and noise levels are sufficient to recover the intrinsic lag reliably.

Figure 5 shows the distribution of recovered-to-input lag ratios from the ICCF simulations. The distributions are strongly centered around unity, confirming that the input lags can be accurately recovered under the actual cadence and noise conditions. These results validate the significance and reliability of our measured lags for both Hβ and Hα in Mrk 1048 and Mrk 618.

We have also employed the publicly available PyI^{2}CCF code,[19] developed by H. Guo et al. (2022) and based on the method described by V. U et al. (2022). This approach evaluates the statistical significance of the lag measurements and provides an independent check on the reliability of the ICCF method. The method is grounded on the null hypothesis that, when two uncorrelated random light curves are cross-correlated, the maximum correlation coefficient ($r_{\rm max}$) should be greater than or equal to the observed value $r_{\rm max,obs}$ obtained from the actual light curves. To test this, the code generates a large ensemble of mock light curves from a DRW model with the same noise properties and cadence as the observed data (see also S. Pandey et al. 2022; V. U et al. 2022; D. H. González-Buitrago et al. 2023; J.-H. Woo et al. 2024). In this work, we generated 5000 mock realizations of the continuum, Hβ, and Hα light curves. The resulting lag measurements and their significance are summarized in Table 3. Alongside the ICCF and JAVELIN results, the PyI^{2}CCF lag values and the corresponding p-values for the null hypothesis are reported. Following the reliability criteria $p \leqslant 0.2$ (H. Guo et al. 2022; V. U et al. 2022; J.-H. Woo et al. 2024) and $r_{\rm max} > 0.5$, we confirm that all lag measurements listed in Table 3 are robust. Notably, $r_{\rm max}$ values remain in the range 0.7–0.9, further supporting the reliability of the ICCF results.

5. Effect of Detrending

In our analysis, a linear trend is apparent in the light curves of Mrk 1048, while it is less pronounced in Mrk 618. To account for this, we applied a linear detrending procedure by fitting a straight line to both the continuum and emission-line light curves and subtracting the best-fit model from the original data. This approach isolates short-term intrinsic variability while minimizing the impact of long-term drifts (see, e.g., Z.-X. Zhang et al. 2019; J.-H. Woo et al. 2024), without introducing artificial fluctuations that could arise from higher-order polynomial fits. The detrended light curves and corresponding lag measurements are shown in Figure A1 in the Appendix. Time lags were re-estimated using both ICCF and JAVELIN, and the results are summarized in Table A1. The posterior lag distributions displayed in Figure A1 exhibit broader spreads or multiple peaks in some cases, reflecting weaker correlations. Consistently, the maximum cross-correlation coefficients ($r_{\rm max}$) decrease across all cases—dropping to $\leqslant$0.6 for Mrk 1048 and below 0.3 for Mrk 618. To further evaluate the statistical significance of these lags, we employed PyI^{2}CCF, with the corresponding p-values for the null hypothesis listed in Table A1. For Mrk 1048, the p-values exceed 0.25, while for Mrk 618 they are even higher (up to 0.72 for the correlation of g-band versus Hα), indicating that detrending substantially reduces the significance of the apparent lag. The detrended results are discussed in the Appendix; however, due to their lower significance, these lags were not adopted as our final measurements.

6. Black Hole Mass Measurement

6.1. Mean and rms Spectrum

We constructed the mean spectrum and the rms spectrum using the following definitions:

$$F\bar{(\lambda)} = \frac{1}{N}\sum_{i=0}^{N-1} F_i(\lambda) \tag{3}$$

and

$$S(\lambda) = \sqrt{\frac{1}{N-1}\sum\nolimits_{i=1}^{N}(F_i(\lambda) - F\bar{(\lambda)}^2)} \tag{4}$$

where $F_i(\lambda)$ represents the ith spectrum in a set of $N = 25$ spectra collected during the monitoring campaign for each source.

The mean spectrum ($\bar{F}(\lambda)$) represents the average flux at each wavelength across all epochs and typically exhibits a high S/N. In contrast, the rms spectrum ($S(\lambda)$) characterizes the variability at each wavelength, highlighting regions with significant temporal changes in flux. For the final rms spectrum, we subtracted the contribution from measurement noise by estimating the observed variance at each wavelength and removing the average noise variance. This was carried out with inverse-variance weighting across epochs to account for differing uncertainties. To quantify the reliability of the rms spectrum, bootstrap resampling was used to estimate the 1σ uncertainties, providing robust confidence intervals on the intrinsic variability. Figure 6 shows the mean and rms spectra for Mrk 1048 and Mrk 618 in the left and right panels, respectively. In each panel, solid and dotted lines denote the spectra before and after subtraction of the power-law continuum. Prominent emission-line regions are visible in both panels. The mean spectrum, benefiting from higher S/N, reveals strong features including both narrow and broad emission lines. The rms spectrum, while having lower S/N, also displays narrow emission lines that ideally should be absent. This is likely due to the use of data from different instruments and telescopes, where factors such as spectral alignment, instrumental resolution, and seeing conditions during observations can significantly impact the construction of the rms spectrum. Consequently, as shown in Figure 6, both sources exhibit [O III] emission lines, which are more prominent in Mrk 618 than in Mrk 1048. The rms spectrum of Mrk 1048 closely resembles that presented by V. U et al. (2022). Although noisier, the rms spectrum effectively isolates variable components by suppressing contributions from nonvarying features such as narrow emission lines and host-galaxy starlight. This makes it a valuable diagnostic for identifying intrinsically variable broad-line components. However, due to its lower signal-to-noise ratio and sensitivity to noise fluctuations, measuring emission line widths from the rms spectrum remains challenging.

6.2. Line Width and Black Hole Mass Measurement

To measure the black hole masses, we measured the FWHM and the line dispersion ($\sigma_{\rm line}$) of the Hβ and Hα emission lines from both the mean and rms spectra after continuum subtraction. The FWHM was calculated by identifying the wavelengths corresponding to 50% of the maximum flux on the blue and red sides of the emission line profile, denoted as λ_l and λ_r, respectively. The FWHM is then obtained as the difference $\lambda_r - \lambda_l$ (B. M. Peterson et al. 2004). To compute the line dispersion, we first determined the flux-weighted centroid

---

[19] https://github.com/legolason/PyIICCF/

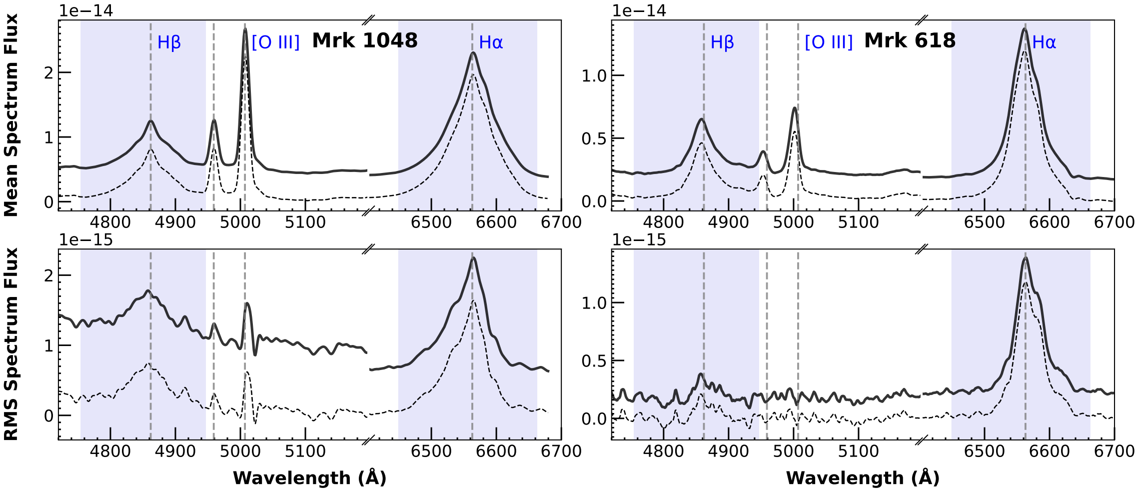

Figure 6. The mean and rms spectra for Mrk 1048 (left) and Mrk 618 (right). The solid lines indicate the original spectrum, while the dotted lines are the continuum-subtracted spectrum.

of the line using the expression

$$\lambda_0 = \frac{\int \lambda f_\lambda \, d\lambda}{\int f_\lambda \, d\lambda} \tag{5}$$

then calculated the second moment of the profile as

$$\sigma_{\rm line}^2 = \frac{\int \lambda^2 f_\lambda \, d\lambda}{\int f_\lambda \, d\lambda} - \lambda_0^2. \tag{6}$$

Assuming that the motion of the BLR gas is dominated by the gravitational potential of the central black hole, we measured the black hole mass using the virial relation from Equation (1). We adopted a scaling factor $f = 4.47$ for line dispersion-based measurements, and $f = 1.12$ for those based on FWHM (J. H. Woo et al. 2015). To estimate the uncertainties in the emission-line widths and, consequently, the black hole mass, we employed a Monte Carlo bootstrap method following the approach of B. M. Peterson et al. (2004). For each realization, N spectra were randomly selected with replacement from the original set of N nightly spectra, from which the mean and rms spectra were reconstructed. Similarly, for the continuum regions adjacent to each emission line, we incorporated their flux uncertainties into the analysis. At every Monte Carlo realization, the continuum level was randomly varied within its measured error range and then subtracted from the emission-line region. This step is important because the exact placement of the continuum directly affects the shape and strength of the residual emission line. By explicitly including this uncertainty, we ensure that errors arising from imperfect determination of the continuum are consistently carried into the final estimates of the emission-line width. Consequently, the derived values of FWHM and $\sigma_{\rm line}$ reflect not only the random noise present in the spectra but also the systematic uncertainty associated with continuum subtraction, providing a more realistic and reliable error budget. For Hβ and Hα, the continuum sidebands were randomly varied within ±10 Å (A. J. Barth et al. 2015) of the nominal windows ([4780, 4940] Å for Hβ and [6450, 6680] Å for Hα). A total of 5000 realizations were generated, each yielding a perturbed line profile from which both FWHM and $\sigma_{\rm line}$ were measured. The median of the resulting distributions was adopted as the final value of the line width, and the 16th and 84th percentiles defined the 1σ confidence interval. The instrumental resolution was also subtracted from the obtained FWHM and $\sigma_{\rm line}$. The uncertainty in black hole mass measurement is measured by propagating the errors of lag $\tau \pm \sigma_\tau$ and line width $\Delta V \pm \sigma_{\Delta V}$. These values were consistently used to measure the black hole masses from the mean and rms spectra. We used the lag values derived from the ICCF method to measure the black hole masses for both sources. Table 4 presents the results of black hole mass measurements based on both the Hα and Hβ emission lines, using line widths obtained from the mean and rms spectra. The line widths are resolution-corrected with respect to ADFOSC and HFOSC instrumental resolution.

Table 4

Hβ and Hα Line Widths and Black Hole Mass Measurements with Lower and Upper Limits

Source (1)	Line (2)	FWHM (km s^{-1}) (3)	$M_{\rm BH}$ ($\times 10^7\,M_\odot$) (4)	$\sigma_{\rm line}$ (km s^{-1}) (5)	$M_{\rm BH}$ ($\times 10^7\,M_\odot$) (6)
Mean spectrum measurements					
Mrk 1048	Hβ	4677^{+276}_{-268}	$4.81^{+1.5}_{-1.6}$	2193^{+45}_{-47}	$4.23^{+1.3}_{-1.4}$
	Hα	3643^{+186}_{-174}	$5.42^{+1.5}_{-1.6}$	1817^{+27}_{-26}	$5.40^{+1.5}_{-1.5}$
Mrk 618	Hβ	2261^{+128}_{-139}	$1.15^{+0.4}_{-0.3}$	1499^{+49}_{-55}	$1.75^{+0.6}_{-0.5}$
	Hα	2113^{+134}_{-83}	$1.36^{+0.4}_{-0.7}$	1327^{+21}_{-20}	$2.15^{+0.6}_{-0.9}$
rms spectrum measurements					
Mrk 1048	Hβ	4975^{+260}_{-251}	$5.71^{+1.7}_{-1.4}$	2678^{+71}_{-77}	$6.30^{+2.0}_{-2.1}$
	Hα	3333^{+211}_{-234}	$4.54^{+1.3}_{-1.3}$	1716^{+63}_{-61}	$4.81^{+1.3}_{-1.4}$
Mrk 618	Hβ	2172^{+139}_{-136}	$1.06^{+0.4}_{-0.3}$	832^{+44}_{-69}	$0.62^{+0.2}_{-0.2}$
	Hα	2335^{+113}_{-99}	$1.67^{+0.5}_{-0.8}$	987^{+61}_{-63}	$1.19^{+0.4}_{-0.6}$

Note. Columns are (1) object name, (2) the line used for calculations, (3) the FWHM of the emission line in km s^{-1}, (4) the black hole mass measured using the FWHM, (5) $\sigma_{\rm line}$ (km s^{-1}), the line dispersion (second moment) of the emission line profile, and (6) black hole mass measured using $\sigma_{\rm line}$. Black hole masses are in units of $10^7\,M_\odot$.

In the case of Mrk 1048, black hole mass measures for the Hβ emission line are between $4.81^{+1.5}_{-1.6} \times 10^7 M_\odot$ and

$5.71^{+1.7}_{-1.4} \times 10^7 M_{\odot}$ considering FWHM based on the mean and rms spectra, respectively. Additionally, using $\sigma_{\rm line}$ defined from Equation (6) as an estimator of line width, the black hole mass is from $4.23^{+1.3}_{-1.4} \times 10^7 M_{\odot}$ to $6.30^{+2.0}_{-2.1} \times 10^7 M_{\odot}$. For H$\alpha$ emission line, the black hole mass with FWHM is in the range from $4.54^{+1.3}_{-1.3} \times 10^7 M_{\odot}$ to $5.42^{+1.5}_{-1.6} \times 10^7 M_{\odot}$ and from $4.81^{+1.3}_{-1.4} \times 10^7 M_{\odot}$ to $5.40^{+1.5}_{-1.5} \times 10^7 M_{\odot}$ with $\sigma_{\rm line}$. Notably, the FWHM and $\sigma_{\rm line}$ of the Hβ line are broader than those of Hα, consistent with previous findings that Hβ tends to trace higher-velocity gas in the BLR (e.g., J. E. Greene & L. C. Ho 2005; S. Wang et al. 2019). This trend becomes more evident in the rms spectrum. The broader line widths seen in the rms spectra than in the mean spectra may result from the reduced signal-to-noise ratio at the line wings in the mean spectrum, which can lead to underestimation of the true line width.

For Mrk 618, the emission line widths are generally narrower than those of Mrk 1048. From the mean spectrum, for the Hβ emission line, the black hole mass ranges from $1.15^{+0.4}_{-0.3} \times 10^7 M_{\odot}$ and $1.75^{+0.6}_{-0.5} \times 10^7 M_{\odot}$ using FWHM and $\sigma_{\rm line}$, respectively. For the Hα emission line, the black hole mass for Mrk 618 is measured to be $1.36^{+0.4}_{-0.7} \times 10^7 M_{\odot}$ and $2.15^{+0.6}_{-0.9} \times 10^7 M_{\odot}$, respectively. Similarly, for the rms spectrum, the masses are $1.06^{+0.4}_{-0.3} \times 10^7 M_{\odot}$ and $0.62^{+0.2}_{-0.2} \times 10^7 M_{\odot}$ for Hβ, whereas they are $1.67^{+0.5}_{-0.8} \times 10^7 M_{\odot}$ and $1.19^{+0.4}_{-0.6} \times 10^7 M_{\odot}$ for Hα, respectively using FWHM and $\sigma_{\rm line}$.

It is important to note that single-epoch black hole mass estimates are sensitive to the choice of line width used in the virial equation. While FWHM is commonly adopted in single-epoch mass measurements, RM studies involving multiple emission lines have shown that $\sigma_{\rm line}$ offers a more reliable estimator of the virial velocity (B. M. Peterson et al. 2004). Since the rms spectrum effectively isolates variable components by removing nonvarying features such as narrow emission lines and host-galaxy contributions, it is generally more robust for black hole mass estimation. Therefore, we adopt the $\sigma_{\rm line}$ measurements from the rms spectra as our preferred measures of black hole mass. Hence, the black hole mass of Mrk 1048 is $6.30^{+2.0}_{-2.1} \times 10^7 M_{\odot}$ as measured using Hβ and $4.81^{+1.3}_{-1.4} \times 10^7 M_{\odot}$ using Hα emission lines, whereas for Mrk 618 the mass is calculated as $6.2^{+2.0}_{-2.0} \times 10^6 M_{\odot}$ and $1.19^{+0.4}_{-0.6} \times 10^7 M_{\odot}$ using Hβ and Hα emission, respectively.

7. Discussion

7.1. Size–Luminosity Relation

Mrk 1048 was previously monitored as part of the LAMP 2016 campaign (V. U et al. 2022) measuring an Hβ rest-frame time lag of $\tau_{\rm cent} = 9.0^{+9.4}_{-7.4}$ days and $r_{\rm max} = 0.6$. In comparison, our monitoring spanning 2022 October to 2023 March yielded a rest-frame Hβ lag of $10.5^{+2.6}_{-4.2}$ days and a higher $r_{\rm max} = 0.9$. In a more recent effort, C. Sobrino Figaredo et al. (2025) included Mrk 1048 (NGC 985) in a large-scale photometric RM campaign using a narrow band targeting the Hα emission line in nearby Seyfert galaxies ($0.015 < z < 0.05$). For Mrk 1048, they obtained a single-epoch spectrum and modeled the broad Hα emission line. Using their refined photometric RM formalism, they derived a rest-frame Hα time lag of 21.3 ± 0.7 days, which is comparable with our measured rest-frame lag of $18.7^{+5.3}_{-5.4}$ days.

Mrk 618 was previously observed in a 2012 RM campaign by G. De Rosa et al. (2018), where no significant Hβ lag was detected due to a shorter monitoring period. In contrast, the recent multiyear campaign by T. E. Zastrocky et al. (2024) reported lag detections across four seasons (2019–2023), with Hβ lags ranging from $9.2^{+1.6}_{-2.3}$ to $30.9^{+10.6}_{-7.2}$ days. The strongest signal occurred in Season 2, whereas the lag of Season 3 was deemed less reliable due to a dual-peaked cross-correlation function. Our current RM campaign independently confirms a strong reverberation signature in Mrk 618. We detect a rest-frame time lag of $10.2^{+3.4}_{-2.9}$ days (ICCF) for the g band versus Hβ and $14.4^{+4.6}_{-10.5}$ days for the g band versus Hα (Table 3), which are consistent with the best lag value of $15.2^{+2.4}_{-2.3}$ reported by the MAHA campaign in their Season 4 observations. These results reaffirm the presence of a responsive BLR in Mrk 618.

We placed Mrk 1048 and Mrk 618 on the Hβ-based BLR size–luminosity ($R_{\rm BLR}$–L_{5100}) plot using the empirical relation

$$\log\left(\frac{R_{\rm BLR}}{\text{lt-day}}\right) = K + \alpha \log\left(\frac{\lambda L_{\lambda}(5100\ \text{Å})}{10^{44}\quad \text{erg s}^{-1}}\right) \qquad (7)$$

where the slope $\alpha = 0.41$ and intercept $K = 1.45$ with intrinsic scatter 0.32 dex, as calibrated by Y. Shen et al. (2024, hereafter S2024) and with slope $\alpha = 0.402$ and intercept $K = 1.405$ by J.-H. Woo et al. (2024, hereafter W2024) with intrinsic scatter 0.23 dex. For Mrk 1048, with $L_{5100} = 8.30 \times 10^{43}$ erg s^{-1}, the predicted Hβ BLR sizes are $R_{\rm BLR} = 26.2$ lt-day (S2024) and 23.6 lt-day (W2024), whereas our RM measurement yields a smaller lag of 10.5 lt-day. In contrast, for Mrk 618, with $L_{5100} = 2.71 \times 10^{43}$ erg s^{-1}, the predicted sizes are 16.5 lt-day (S2024) and 15.1 lt-day (W2024), while our measured lag is comparable at 10.2 lt-day. These discrepancies are within the 1σ limit from the global $R_{\rm BLR}$–L_{5100} relation for Mrk 1048. This is visualized in Figure 7.

Correcting for host-galaxy contamination is essential for accurately determining AGN luminosities, as it significantly impacts the size–luminosity relation and can introduce substantial uncertainties if unaccounted for. We applied the empirical host-fraction relation from P. Jalan et al. (2023), which is based on the measurement of host contamination from SDSS spectra, and estimated host contributions of ∼43.7% for Mrk 1048% and ∼57.4% for Mrk 618. This yields host-subtracted AGN continuum luminosities of $L_{5100,\rm AGN} \approx 4.67 \times 10^{43}$ erg s^{-1} and $\approx 1.15 \times 10^{43}$ erg s^{-1}, respectively. Recalculating the expected BLR sizes with these corrected values, we obtain $R_{\rm BLR} = 20.6$ and 18.8 lt-day (S2024 and W2024, respectively) for Mrk 1048, and 11.6 and 10.7 lt-day for Mrk 618.

To cross-check our spectrophotometric Hα lag measurements, we estimated the BLR sizes using the directly measured 5100 Å continuum luminosities and the Hα-based $R_{\rm BLR}$–L_{5100} relations from H. Cho et al. (2023, hereafter C2023) and C. Sobrino Figaredo et al. (2025, hereafter S2025). For this, we used Equation (7) for the Hα emission line with $K = 1.51$, $\alpha = 0.57$, and scatter = 0.32 dex based on S2025, and $K = 1.59$, $\alpha = 0.58$, with scatter = 0.31 dex based on C2023. Using the total luminosities, the predicted BLR sizes for Mrk 1048 are 34.8 and 29.1 lt-day (C2023 and S2025, respectively), compared to our measured lag of 18.7 lt-day. For Mrk 618, the predictions are 18.2 and 15.4 lt-day, while our

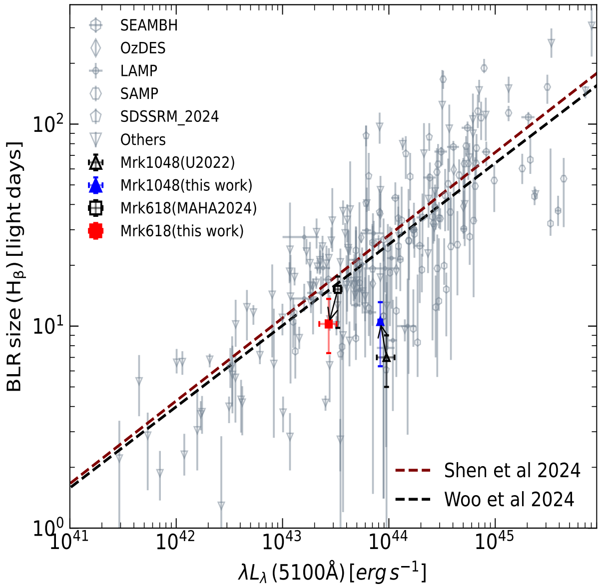

Figure 7. The relationship between the Hβ BLR size and the optical continuum luminosity at 5100 Å. A range of reverberation-mapped AGN samples from the literature are overplotted for comparison. These include SEAMBHs (P. Du et al. 2016, 2018; C. Hu et al. 2021; S.-S. Li et al. 2021, gray open circles), SDSSRM-2024 sources (Y. Shen et al. 2024, gray open squares), OzDES AGNs (U. Malik et al. 2023, gray open diamonds), LAMP sources (V. U et al. 2022, gray open circles), and SAMP sources (J.-H. Woo et al. 2024, gray open hexagons). Additional RM sources from various studies (M. C. Bentz et al. 2013; S. Park et al. 2017; S. Rakshit et al. 2019; E. D. Bontà et al. 2020; S. Rakshit 2020; S. Pandey et al. 2022, gray open inverted triangles) are also included. The maroon and black dashed lines represent the best-fit *R*–*L* relation as reported by J.-H. Woo et al. (2024) and Y. Shen et al. (2024), respectively. Our target sources, Mrk 1048 and Mrk 618, are marked with a filled blue triangle and a filled red circle, respectively. Mrk 1048 moves toward the upper left, while Mrk 618 moves toward the lower left, to the best-fit relation. These are still lying closer to the best-fit relation.

measured lag is comparable at 14.4 lt-day. Applying host-galaxy correction, the AGN-only 5100 Å luminosities yield revised $R_{\rm BLR}$ values of 25.1 and 21.0 lt-day (C2023 and S2025, respectively) for Mrk 1048, and 11.2 and 9.5 lt-day for Mrk 618. The Mrk 1048 value is within a factor of ∼1.2, and Mrk 618 shows a factor of ∼1.4 times longer measured lag than predicted from the Hα-based $R_{\rm BLR}$–L_{5100} relation. This is shown in Figure 8, consistent with the deviation observed in the Hβ-based scaling.

The standard $R_{\rm BLR}$–L_{5100} relation tends to overpredict the BLR sizes of high-accretion AGNs with strong Fe II emission. P. Du & J.-M. Wang (2019) proposed a refined relation incorporating the relative Fe II strength, $R_{\rm FeII} = {\rm EW}_{\rm FeII}/{\rm EW}_{{\rm H}\beta}$, showing that higher $\rm R_{FeII}$ values correspond to shorter Hβ lags at fixed luminosity. For Mrk 618, we measure $R_{\rm FeII} \approx 1.50$, suggesting a predicted BLR size below 7 lt-day. However, our measured Hβ lag is slightly longer at ∼10.2 lt-day, indicating that Mrk 618 deviates minimally from this trend.

7.2. Stratification of BLR

We computed the ratio of Hα to Hβ lags to assess the ionization stratification of the BLR in our sources. For Mrk 1048, this ratio is

$$\frac{\tau_{{\rm H}\alpha}}{\tau_{{\rm H}\beta}} = \frac{18.7^{+5.3}_{-5.4}}{10.5^{+2.6}_{-4.2}} \approx 1.7^{+0.6}_{-0.9}, \tag{8}$$

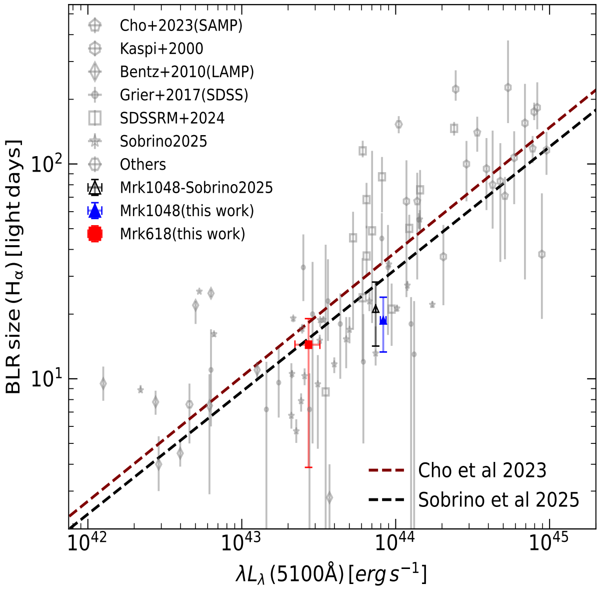

Figure 8. The relationship between the Hα BLR size and the monochromatic continuum luminosity at 5100 Å. Reverberation-mapped sources with Hα lag measurements from previous studies are overplotted for comparison, including those from S. Kaspi et al. (2000), M. C. Bentz et al. (2010), C. J. Grier et al. (2017), H. Cho et al. (2020), J.-H. Woo et al. (2024), C. Sobrino Figaredo et al. (2025), and Y. Shen et al. (2024), along with additional sources from S. G. Sergeev et al. (2016), H.-C. Feng et al. (2021), and S.-S. Li et al. (2022). The maroon and black dashed lines represent the best-fit *R*–*L* relation as derived by H. Cho et al. (2023) and C. Sobrino Figaredo et al. (2025), respectively. Our target AGNs, Mrk 1048 and Mrk 618, are plotted as a filled blue triangle and a filled red circle, respectively. The previous measure of Hα for Mrk 1048 (C. Sobrino Figaredo et al. 2025) is also marked with an open triangle. Mrk 618 lies closer to the Hα best-fit relation, while Mrk 1048 is slightly more offset than found by C. Sobrino Figaredo et al. (2025).

and for Mrk 618

$$\frac{\tau_{{\rm H}\alpha}}{\tau_{{\rm H}\beta}} = \frac{14.4^{+4.6}_{-10.5}}{10.2^{+3.4}_{-2.9}} \approx 1.4^{+0.6}_{-1.1}. \tag{9}$$

These ratios indicate that in Mrk 1048, the Hα-emitting region lies farther out in the BLR than the Hβ-emitting region, consistent with expectations from photoionization stratification. In contrast, the ratio for Mrk 618 suggests a more cospatial origin of the two lines, potentially linked to a flatter radial ionization profile or more compact BLR geometry.

Our result for Mrk 1048 notably contrasts with the value of $\tau_{{\rm H}\alpha}/\tau_{{\rm H}\beta} = 2.9^{+1.4}_{-1.1}$ reported by S2025, who adopted the Hβ lag of $\tau_{{\rm H}\beta} = 7.4^{+9.7}_{-9.4}$ days from V. U et al. (2022) and derived a rest-frame Hα lag of 21.3 ± 0.7 days. Their reported ratio was among the highest in their sample and interpreted as strong evidence for radial stratification in the BLR. In contrast, our updated measurements yield a more moderate ratio of $\tau_{{\rm H}\alpha}/\tau_{{\rm H}\beta} \approx 1.7^{+0.6}_{-0.9}$, which lies closer to the average and median values reported in the literature. Specifically, S2025 reported a mean Hα/Hβ lag ratio of 1.6 ± 0.8 and a median of 1.3 ± 0.8 across their full sample, consistent with earlier studies by S. Kaspi et al. (2000), M. C. Bentz et al. (2010), and Y. Shen et al. (2024), which reported average ratios around 1.4. Our revised result thus falls well within this statistically expected range, suggesting that high-ratio estimates of S2025 may have been inflated due to sparse cadence, low signal-to-noise ratio, or systematics in nonuniform spectral sampling. This reinforces the value of dedicated, well-calibrated, and high-cadence monitoring campaigns in accurately tracing BLR stratification.

Furthermore, our measured ratio for Mrk 1048 is more consistent with the typical range of 1.2–1.8 found by C2023 for high-luminosity AGNs using a recalibrated Hα–Hβ BLR structure analysis. This comparison underscores the importance of uniform and simultaneous spectral monitoring for reliably interpreting BLR stratification and dynamics.

7.3. Black Hole Masses

Mrk 1048. Line width comparisons show that while V. U et al. (2022) found $\mathrm{FWHM_{mean}} = 4830 \pm 80$ km s^{-1} and $\sigma_{\rm mean} = 1840 \pm 58$ km s^{-1}, our results are $\mathrm{FWHM_{mean}} = 4677^{+276}_{-268}$ km s^{-1} and $\sigma_{\rm mean} = 2193^{+45}_{-47}$ km s^{-1}. However, our broader rms spectrum values ($\mathrm{FWHM_{rms}} = 4975^{+260}_{-251}$ km s^{-1}, $\sigma_{\rm rms} = 2678^{+71}_{-77}$ km s^{-1}), when compared to those from the LAMP campaign (4042 ± 406 km s^{-1} and 1726 ± 76 km s^{-1}), indicate that our data captured a larger portion of the line variability, possibly tracing higher-velocity components of the BLR. Consequently, the black hole mass measured by V. U et al. (2022) using the rms $\sigma_{\rm line}$ was $2.2 \times 10^7 M_\odot$, which is significantly lower than our result of $6.30 \times 10^7 M_\odot$, a factor of $\sim$3 difference. Additionally, our directly measured continuum luminosity at 5100 Å is $(8.30 \pm 0.35) \times 10^{43}$ erg s^{-1}, consistent with the $(9.5 \pm 1.8) \times 10^{43}$ erg s^{-1} reported by V. U et al. (2022). The difference in the black hole mass estimate could be due to a lack of host-galaxy correction, differences in variability in the two monitoring campaigns, and broader line width measurement. While V. U et al. (2022) identified infalling BLR kinematics using velocity-resolved RM, we were not able to perform such an analysis due to the limited number of epochs in our campaign. C. Sobrino Figaredo et al. (2025) reported a black hole mass of $M_{\rm BH} = 9.12^{+0.30}_{-0.34} \times 10^7 M_\odot$ using the FWHM of the Hα line. Our mass measurement is in closer agreement with theirs. Their host-subtracted continuum luminosity at 5100 Å was derived using the flux variation gradient method, while the Eddington ratio of 0.109 (which is closer to our estimate of 0.094) was computed via Fe II emission line strength. The slight discrepancy in mass measurement may stem from differences in the method used for BLR size measurement (their photometric RM compared to our spectroscopic RM), the treatment of emission line width, single-epoch assumptions, or line modeling details.

Mrk 618. The integrated line widths derived from our spectra yield FWHM values of 2261^{+128}_{-139} km s^{-1} (mean) and 2172^{+139}_{-136} km s^{-1} (rms) for Hβ, and corresponding $\sigma_{\rm line}$ values of 1499^{+49}_{-55} km s^{-1} and 832^{+44}_{-69} km s^{-1}. These values are slightly smaller than the range of FWHM = 2387–3219 km s^{-1} and $\sigma_{\rm line}$ = 1279–1650 km s^{-1} reported by MAHA. Additionally, our Hα measurements display consistent broadening behavior, indicating a stable BLR geometry across multiple lines and epochs. Furthermore, our decomposition of the Hβ profile reveals a mild asymmetry that leans toward the blue wing, which aligns with the findings of the MAHA campaign, which show evolving line asymmetry across seasons. Specifically, MAHA reported Hβ asymmetry values ranging from -0.256 to -0.144, suggesting a shift from disk-like dynamics (Season 2) to an outflow-dominated geometry (Season 4). While we do not perform velocity-resolved lag measurements in our current dataset, the presence of asymmetry in the line profiles hints at similar kinematic complexities. Our directly measured continuum luminosity at 5100 Å is $(2.72 \pm 0.50) \times 10^{43}$ erg s^{-1}, which reduces to 1.15×10^{43} erg s^{-1} after correcting for the host-galaxy contribution, which is lower than the MAHA Season 4 value of $(3.31 \pm 0.28) \times 10^{43}$ erg s^{-1}. The decreasing trend in L_{5100} across the MAHA seasons from 4.73×10^{43} to 3.31×10^{43} erg s^{-1} is aligned with the lower luminosity recorded in our campaign, further supporting the observed decline in AGN activity.

7.4. Implication of SARM Observation

To estimate the angular extent of the BLR, we used our directly measured BLR radii from Hβ and Hα time lags, along with angular diameter distances derived under a standard ΛCDM cosmology ($H_0 = 70$ km s^{-1} Mpc^{-1}, $\Omega_M = 0.3$, $\Omega_\Lambda = 0.7$). The angular size was calculated using the relation

$$\xi_{\rm BLR} = \frac{R_{\rm BLR}}{D_A}, \tag{10}$$

where $R_{\rm BLR}$ is the BLR radius in parsecs, and D_A is the angular diameter distance in megaparsecs. The resulting angular size was then converted to microarcseconds (μas).

For Mrk 1048, our measured Hβ and Hα lags of $10.5^{+2.6}_{-4.2}$ and $18.7^{+5.3}_{-5.4}$ lt-day correspond to BLR radii of $0.0085^{+0.0020}_{-0.0034}$ pc and $0.0152^{+0.0043}_{-0.0044}$ pc, given that 1 lt-day $\approx$ 0.0008 pc, adopting a redshift of $z = 0.043$. With an angular diameter distance of $D_A = 168.0$ Mpc, the angular sizes are $\xi_{\rm BLR} \approx 10.1^{+2.4}_{-4.0}$ μas (Hβ) and $15.5^{+4.4}_{-4.5}$ μas (Hα). For Mrk 618 ($z = 0.034$), our Hβ and Hα lags of $10.2^{+3.4}_{-2.9}$ and $14.4^{+4.6}_{-10.5}$ lt-day yield BLR radii of $0.0083^{+0.0027}_{-0.0024}$ pc and $0.0117^{+0.0038}_{-0.0085}$ pc, respectively. With $D_A = 137.1$ Mpc, the corresponding angular sizes are $\xi_{\rm BLR} \approx 12.6^{+4.1}_{-3.5}$ μas (Hβ) and $17.1^{+5.4}_{-10.1}$ μas (Hα).

These angular sizes are generally smaller than those predicted by J.-M. Wang et al. (2020), who report, for instance, $\xi_{\rm BLR} = 46.4$ μas for Mrk 1048 based on an assumed BLR size of 48.6 lt-day. The discrepancy likely reflects differences in BLR size measurements across epochs and methods. Nonetheless, the scales we derive remain within the reach of the interferometric resolution of GRAVITY.

The Paα emission line ($\lambda_{\rm rest} = 1.875$ μm), commonly used in SA, is redshifted to 1.956 μm for Mrk 1048, which lies around the window edge within GRAVITY's K-band coverage (1.95–2.45 μm). However, for Mrk 618, the redshifted Paα line appears at 1.94 μm, just outside the lower limit of this band, limiting its accessibility. In such cases, alternative broad emission lines such as Brγ ($\lambda_{\rm rest} = 2.17$ μm), He I (2.06 μm), H_2 1–0 S(1) (2.12 μm), and [Si VI] (1.96 μm) are viable options. For both Mrk 1048 and Mrk 618, these lines redshift to within the K-band window and offer promising alternatives, but are challenging for spatially resolving the BLR kinematics using GRAVITY/GRAVITY+.

To improve SARM measurements, efforts should be made to achieve better consistency and reduce systematic uncertainties in the data (see J.-M. Wang et al. 2020). A key improvement would be the use of the same broad emission line, such as Paα or Hβ, in both SARM observations, ensuring that both methods probe the same physical region of the BLR. Although one of the goals of our campaign was to observe the infrared lines, the number of such epochs is too few to perform a detailed investigation for the lag measurement. Additionally, conducting these observations (RM and SA) jointly or within the dynamical timescale of the BLR can minimize biases arising from temporal variations in the BLR structure. Incorporating information from velocity-resolved RM and polarimetry can help constrain key physical parameters such as inclination, opening angle, and the degree of ordered motion in the BLR. Expanding the sample size to include well-monitored AGNs and improving the precision of interferometric phase measurements will further reduce both statistical and systematic errors.

8. Conclusion

We observed the sources Mrk 1048 and Mrk 618 among the seven sources selected from J.-M. Wang et al. (2020) with the aim of performing SARM studies. Our spectrophotometric weekly cadence monitoring of Mrk 1048 and Mrk 618 was conducted between 2022 October and 2023 March using optical and near-IR instruments such as ADFOSC and TANSPEC mounted at the 3.6 m DOT and the HFOSC mounted on the 2 m HCT. Broadband photometric monitoring was done using *V*, *R*, and SDSS *r* filters immediately before spectroscopy. Intercalibrated *g*-band light curves, using ASAS-SN and ZTF data, were adopted as the primary continuum driver after alignment via PyCALI. This work covers the first part of the SARM, i.e., RM analysis. We gathered the following results for Mrk 1048 and Mrk 618.

1. Mrk 1048 shows moderate continuum variability with a fractional variability amplitude ($F_{\rm var}$) of 7.30% in the *g* band, while the Hβ and Hα emission lines exhibit slightly higher variability, at 10.30% and 6.75%, respectively. The corresponding maximum-to-minimum flux ratios ($R_{\rm max}$) are 1.42 (*g* band), 1.50 (Hβ), and 1.27 (Hα). In contrast, Mrk 618 displays a lower continuum variability ($F_{\rm var} \sim 4.20\%$) but a more pronounced variability in its emission lines, with 7.68% for Hβ and a notably higher 13.91% for Hα. The emission lines in both sources exhibit greater flux variability than the continuum, consistent with expectations for reverberation, and Hα consistently appears stronger and more variable than Hβ in both objects.
2. Using ICCF-based lags and optical luminosities, both sources were placed on the $R_{\rm BLR}$–L_{5100} relation for Hβ and Hα emission lines. For Mrk 1048, the Hβ lag is $10.5^{+2.6}_{-4.2}$ days with $L_{5100} = (8.30 \pm 0.35) \times 10^{43}$ erg s^{-1}, while Hα gives a longer lag of $18.7^{+5.3}_{-5.4}$ days. For Mrk 618, the Hβ and Hα lags are $10.2^{+3.4}_{-2.9}$ and $14.4^{+4.6}_{-10.5}$ days, respectively, with a lower luminosity of $L_{5100} = (2.71 \pm 0.50) \times 10^{43}$ erg s^{-1}. Both sources exhibit deviate mildly but are broadly consistent with the $R_{\rm BLR}$–L_{5100} relation, with Mrk 618 appearing slightly offset in Hβ, but more so in Hα, whereas Mrk 1048 deviates in Hβ but is closer in Hα, reflecting differences in structure or ionization in their BLRs.
3. Black hole mass measurements for Mrk 1048 range from 4.2×10^7 to $6.3 \times 10^7 M_\odot$ with Hβ. For Mrk 618, narrower line widths yield lower masses, ranging from 0.6×10^7 to $1.7 \times 10^7 M_\odot$, depending on the choice of line width and emission line. As $\sigma_{\rm line}$ from rms spectra best isolates the variable BLR component, we adopt these as our preferred values: $6.30^{+2.0}_{-2.1} \times 10^7 M_\odot$ for Mrk 1048 and $1.19^{+0.4}_{-0.6} \times 10^7 M_\odot$ for Mrk 618.

Acknowledgments

S.R. acknowledges partial support from the Science and Engineering Research Board (SERB), Department of Science and Technology (DST), Government of India, through the Start-up Research grant (SRG) No. SRG/2021/001334. J.H. W. acknowledges the support from the Basic Science Research Program through the National Research Foundation of the Korean Government (grant No. NRF-2021R1A2C3008486). A.K.M. acknowledges the support from the European Research Council (ERC) under the European Union’s Horizon 2020 research and innovation program (grant No. 951549). This study makes use of data obtained from the 3.6 m Devasthal Optical Telescope (DOT), a National Facility operated by the Aryabhatta Research Institute of Observational Sciences (ARIES), and the 2 m Himalayan Chandra Telescope (HCT). ARIES is an autonomous institute under the DST, Government of India. We are grateful to the scientific and technical staff at ARIES for their invaluable support during DOT observations. The TIFR-ARIES Near Infrared Spectrometer (TANSPEC) mounted on DOT was developed jointly by TIFR, ARIES, and MKIR, Hawaii. We thank the 3.6 m DOT and IR astronomy teams at TIFR for their assistance during TANSPEC observations. We also acknowledge the support provided by the staff at the Indian Astronomical Observatory (IAO), Hanle, and the CREST facility in Hosakote, both operated by the Indian Institute of Astrophysics (IIA), Bengaluru, for enabling observations with HCT.

Facilities: ARIES:DOT (ADFOSC, TANSPEC), HCT, (HFOSC).

Software: `mapspec` (M. M. Fausnaugh 2017), PyQSOFit (H. Guo et al. 2018), `PyCALI` (Y.-R. Li et al. 2014), PyCCF (B. M. Peterson et al. 1998), JAVELIN (Y. Zu et al. 2011, 2013), PyI^{2}CCF (H. Guo et al. 2022).

Appendix
Analysis of Detrended Light Curve

We detrended the continuum and emission-line light curves by fitting a straight line to each and subtracting the corresponding best-fit model to obtain the residual (detrended) variations as described in Section 5. Figure A1 and Table A1 illustrate the light curves and lag results for the entire campaign after detrending.

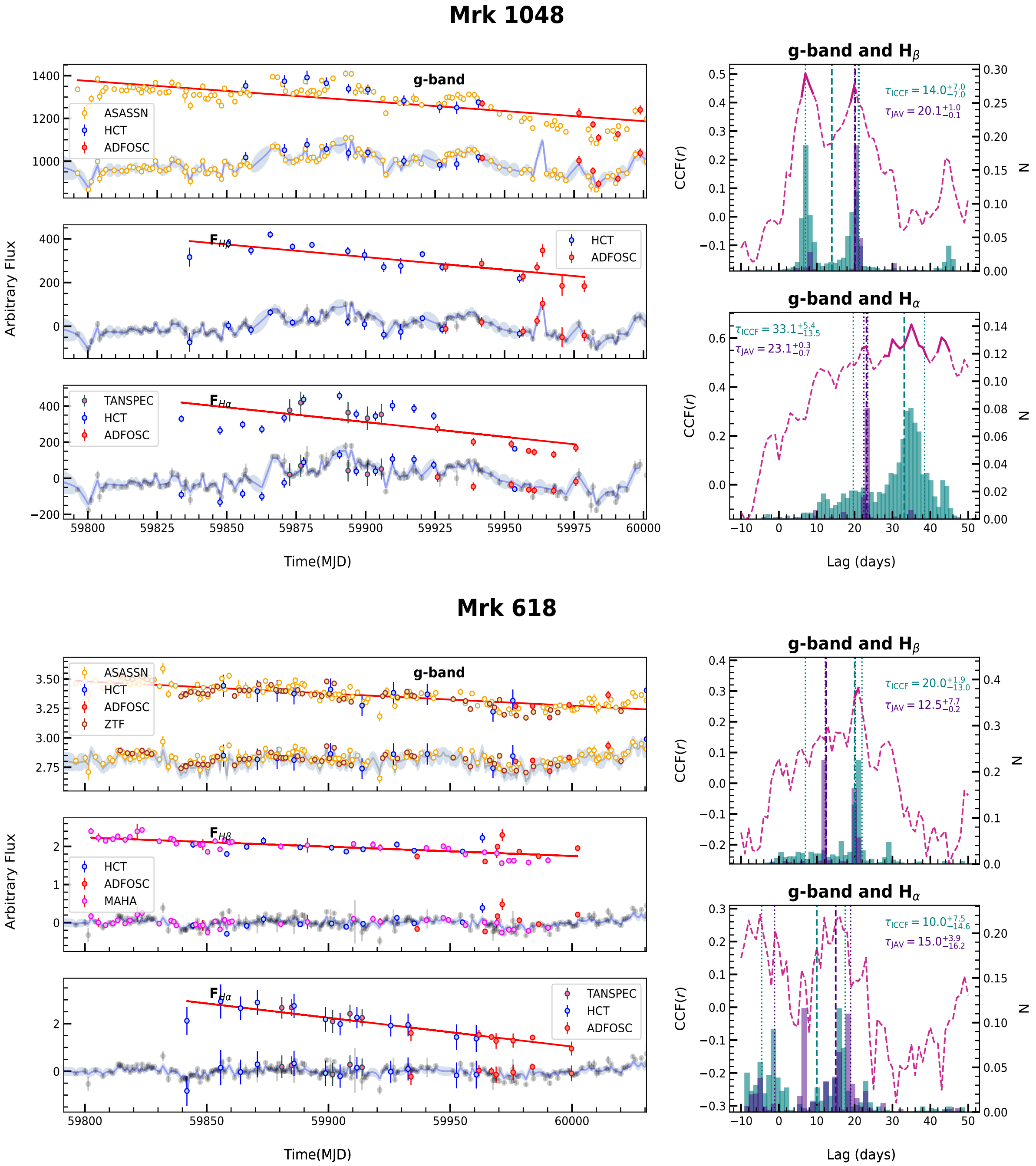

Figure A1. Detrended light-curve analysis for Mrk 1048 and Mrk 618. The top left panel shows the photometric g-band continuum with data points from different telescopes labeled. The middle and bottom left panels display the variations in Hβ and Hα emission-line flux (in arbitrary units), each fitted with a best-fit linear trend shown in red, which has been subtracted to obtain the detrended light curves. The g-band continuum is overlaid for comparison, normalized and shifted to the final adopted lag values listed in Table A1. The JAVELIN model for each light curve is shown in steel blue. The right panels show the corresponding lag distributions from ICCF (teal histograms) and JAVELIN (violet histograms). The magenta dashed curve represents the cross-correlation function, with the left axis showing $r_{\rm max}$ and the right axis showing the probability density N. The darker magenta region marks the central 80% of the CCF peak used to determine the ICCF centroid lag. The vertical dashed lines indicate the 16th and 84th percentile uncertainties of the lag distributions.

Table A1
Detrended Time Delays (Lags) for Mrk 1048 and Mrk 618 using ICCF, JAVELIN, and PyI^{2}CCF

Source	Light Curve	ICCF		JAVELIN	PyI^{2}CCF	
		Lag (days)	$r_{\max}$	Lag (days)	Lag (days)	p-value
(1)	(2)	(3)	(4)	(5)	(6)	(7)
Mrk 1048	g band versus Hβ	$14.0^{+7.0}_{-7.0}$	0.50	$20.1^{+1.0}_{-0.1}$	$16.58^{+5.0}_{-9.1}$	0.30
	g band versus Hα	$33.1^{+5.4}_{-13.5}$	0.62	$23.1^{+0.3}_{-0.7}$	$33.05^{+6.5}_{-11.5}$	0.25
Mrk 618	g band versus Hβ	$20.0^{+1.9}_{-13.0}$	0.30	$12.5^{+7.7}_{-0.2}$	$20.47^{+1.0}_{-10.0}$	0.27
	g band versus Hα	$10.0^{+7.5}_{-14.6}$	0.28	$15.0^{+3.9}_{-16.2}$	$15.0^{+3.0}_{-18.5}$	0.72

Note. All lags here are from *detrended* light curves and are quoted in the observer frame. Columns: (1) source; (2) light-curve pair; (3) ICCF centroid lag; (4) cross-correlation coefficient; (5) JAVELIN lag; (6) PyI^{2}CCF lag; (7) PyI^{2}CCF null-hypothesis p-value.

ORCID iDs

Shivangi Pandey https://orcid.org/0000-0002-4684-3404
Suvendu Rakshit https://orcid.org/0000-0002-8377-9667
S. Muneer https://orcid.org/0000-0002-4024-956X
Yan-Rong Li https://orcid.org/0000-0001-5841-9179
Jian-Min Wang https://orcid.org/0000-0001-9449-9268
C. S. Stalin https://orcid.org/0000-0002-4998-1861
Jong-Hak Woo https://orcid.org/0000-0002-8055-5465
Romain G. Petrov https://orcid.org/0000-0003-4759-6051
James Leftley https://orcid.org/0000-0001-6009-1803
Sebastian F. Hönig https://orcid.org/0000-0002-6353-1111
Amit Kumar Mandal https://orcid.org/0000-0001-9957-6349
Shu Wang https://orcid.org/0000-0002-2052-6400
Michael Brotherton https://orcid.org/0000-0002-1207-0909

References

Amorim, A., Bauböck, M., & Bentz, M.C. 2021, A&A, 654, A85
Bahcall, J. N., Kozlovsky, B.-Z., Salpeter, E. E., et al. 1972, ApJ, 171, 467
Barbary, K. 2016, JOSS, 1, 58
Barth, A. J., Bennert, V. N., Canalizo, G., et al. 2015, ApJS, 217, 26
Bentz, M. C., Denney, K. D., Grier, C. J., et al. 2013, ApJ, 767, 149
Bentz, M. C., Horenstein, D., Bazhaw, C., et al. 2014, ApJ, 796, 8
Bentz, M. C., Walsh, J. L., Barth, A. J., et al. 2010, ApJ, 716, 993
Beroiz, M., Cabral, J., & Sanchez, B. 2020, A&C, 32, 100384
Blandford, R. D., McKee, C. F., Blandford, R. D., & McKee, C. F. 1982, ApJ, 255, 419
Bontà, E. D., Peterson, B. M., Bentz, M. C., et al. 2020, ApJ, 903, 112
Boroson, T. A., & Green, R. F. 1992, ApJS, 80, 109
Cackett, E. M., Bentz, M. C., & Kara, E. 2021, iSci, 24, 102557
Cho, H., Woo, J.-H., Hodges-Kluck, E., et al. 2020, ApJ, 892, 93
Cho, H., Woo, J.-H., Wang, S., et al. 2023, ApJ, 953, 142
De Rosa, G., Fausnaugh, M. M., Grier, C. J., et al. 2018, ApJ, 866, 133
Du, P., Hu, C., Lu, K. X., et al. 2015, ApJ, 806, 22
Du, P., Lu, K.-X., Zhang, Z.-X., et al. 2016, ApJ, 825, 126
Du, P., & Wang, J.-M. 2019, ApJ, 886, 42
Du, P., Zhang, Z.-X., Wang, K., et al. 2018, ApJ, 856, 6
Edelson, R., Gelbord, J., Cackett, E., et al. 2019, ApJ, 870, 123
Elvis, M., & Karovska, M. 2002, ApJ, 581, L67
Fausnaugh, M. M. 2017, PASP, 129, 024007
Fausnaugh, M. M., Grier, C. J., Bentz, M. C., et al. 2017, ApJ, 840, 97
Feng, H.-C., Liu, H. T., Bai, J. M., et al. 2021, ApJ, 912, 92
Fitzpatrick, E. L. 1999, PASP, 111, 63
Gaskell, C. M., & Sparke, L. S. 1986, ApJ, 305, 175
Ghosh, S., Ninan, J. P., Ojha, D. K., & Sharma, S. 2023, JApA, 44, 30
González-Buitrago, D. H., García-Díaz, M. T., Pozo Nuñez, F., & Guo, H. 2023, MNRAS, 525, 4524
Graham, M. J., Kulkarni, S. R., Bellm, E. C., et al. 2019, PASP, 131, 078001
Gravity Collaboration, Amorim, A., Bauböck, M., et al. 2020, A&A, 643, A154
GRAVITY Collaboration, Amorim, A., Bourdarot, G., et al. 2024, A&A, 684, A167
Gravity Collaboration, Sturm, E., Dexter, J., et al. 2018, Natur, 563, 657
Greene, J. E., & Ho, L. C. 2005, ApJ, 630, 122
Grier, C. J., Trump, J. R., Shen, Y., et al. 2017, ApJ, 851, 21
Guo, H., Barth, A. J., & Wang, S. 2022, ApJ, 940, 20
Guo, H., Liu, X., Shen, Y., et al. 2019, MNRAS, 482, 3288
Guo, H., Shen, Y., & Wang, S. 2018, PyQSOFit: Python code to fit the spectrum of quasars, ascl:1809.008
Hu, C., Li, S.-S., Yang, S., et al. 2021, ApJS, 253, 20
Jalan, P., Rakshit, S., Woo, J.-J., Kotilainen, J., & Stalin, C. S. 2023, MNRAS, 521, L11
Kaspi, S., Smith, P. S., Netzer, H., et al. 2000, ApJ, 533, 631
Kelly, B. C., Bechtold, J., & Siemiginowska, A. 2009, ApJ, 698, 895
Kelly, B. C., Becker, A. C., Sobolewska, M., Siemiginowska, A., & Uttley, P. 2014, ApJ, 788, 33
Kochanek, C. S., Shappee, B. J., Stanek, K. Z., et al. 2017, PASP, 129, 104502
Kumar, B., Omar, A., Maheswar, G., et al. 2018, BSRSL, 87, 29
Li, S.-S., Feng, H.-C., Liu, H. T., et al. 2022, ApJ, 936, 75
Li, S.-S., Yang, S., Yang, Z.-X., et al. 2021, ApJ, 920, 9
Li, Y.-R., Hu, C., Yao, Z.-H., et al. 2024, ApJ, 974, 86
Li, Y.-R., Shangguan, J., Wang, J.-M., et al. 2025, ApJ, 988, 42
Li, Y.-R., Songsheng, Y.-Y., Qiu, J., et al. 2018, ApJ, 869, 137
Li, Y.-R., & Wang, J.-M. 2023, ApJ, 943, 36
Li, Y.-R., Wang, J.-M., Hu, C., Du, P., & Bai, J.-M. 2014, ApJL, 786, L6
Malik, U., Sharp, R., Penton, A., et al. 2023, MNRAS, 520, 2009
McHardy, I. M., Koerding, E., Knigge, C., Uttley, P., & Fender, R. P. 2006, Natur, 444, 730
Mushotzky, R. F., Edelson, R., Baumgartner, W., & Gandhi, P. 2011, ApJL, 743, L12
National Optical Astronomy Observatories. 1999, IRAF: Image Reduction and Analysis Facility, Astrophysics Source Code Library, ascl:9911.002
Netzer, H. 2013, The Physics and Evolution of Active Galactic Nuclei (Cambridge Univ. Press)
Omar, A., Kumar, T. S., Krishna Reddy, B., Pant, J., & Mahto, M. 2019, arXiv:1902.05857
Osterbrock, D. E., & Ferland, G. J. 2006, Astrophysics of Gaseous Nebulae and Active Galactic Nuclei (2nd ed.; Univ. Science Books)
Panchal, D., Kumar, T. S., Omar, A., & Misra, K. 2023, JATIS, 9, 018002
Pancoast, A., Brewer, B. J., Treu, T., et al. 2014, MNRAS, 445, 3073
Pandey, S., Rakshit, S., Woo, J.-H., & Stalin, C. S. 2022, MNRAS, 516, 2671
Park, S., Woo, J.-H., Romero-Colmenero, E., et al. 2017, ApJ, 847, 125
Pei, L., Fausnaugh, M. M., Barth, A. J., et al. 2017, ApJ, 837, 131
Peterson, B. M. 1993, PASP, 105, 247
Peterson, B. M., Ferrarese, L., Gilbert, K. M., et al. 2004, ApJ, 613, 682
Peterson, B. M., Wanders, I., Bertram, R., et al. 1998, ApJ, 501, 82
Rakshit, S. 2020, A&A, 642, A59
Rakshit, S., Petrov, R. G., Meilland, A., & Hönig, S. F. 2015, MNRAS, 447, 2420
Rakshit, S., Stalin, C. S., & Kotilainen, J. 2020, ApJS, 249, 17
Rakshit, S., Woo, J.-H., Gallo, E., et al. 2019, ApJ, 886, 93
Rees, M. J. 1984, ARA&A, 22, 471
Rodriguez-Pascual, P. M., Alloin, D., Clavel, J., et al. 1997, ApJS, 110, 9
Schlegel, D. J., Finkbeiner, D. P., & Davis, M. 1998, ApJ, 500, 525
Sergeev, S. G., Nazarov, S. V., & Borman, G. A. 2016, MNRAS, 465, 1898
Sharma, S., Ojha, D. K., Ghosh, A., et al. 2022, PASP, 134, 085002
Shen, Y., Grier, C. J., Horne, K., et al. 2024, ApJS, 272, 26
Shen, Y., Hall, P. B., Horne, K., et al. 2019, A&AS, 241, 34
Shen, Y., Richards, G. T., Strauss, M. A., et al. 2011, A&AS, 194, 45
Sobrino Figaredo, C., Chelouche, D., Haas, M., et al. 2025, ApJS, 276, 48
Tody, D. 1986, SPIE, 627, 733
Tody, D. 1993, ASPC, 52, 173
U, V., Barth, A. J., Vogler, H. A., et al. 2022, ApJ, 925, 52
van Dokkum, P. G. 2001, PASP, 113, 1420

van Groningen, E., & Wanders, I. 1992, PASP, 104, 700
Wang, J.-M., Songsheng, Y.-Y., Li, Y.-R., Du, P., & Zhang, Z.-X. 2020, NatAs, 4, 517
Wang, S., Shen, Y., Jiang, L., et al. 2019, ApJ, 882, 4
Wang, S., & Woo, J.-H. 2024, ApJS, 275, 13
Wang, S., Woo, J.-H., Barth, A. J., et al. 2025, ApJ, 983, 45
Woo, J.-H., & Urry, C. M. 2002, ApJ, 579, 530
Woo, J.-H., Wang, S., Rakshit, S., et al. 2024, ApJ, 962, 67
Woo, J. H., Yoon, Y., Park, S., Park, D., & Kim, S. C. 2015, ApJ, 801, 38
Yu, Z., Kochanek, C. S., Peterson, B. M., et al. 2020, MNRAS, 491, 6045
Zastrocky, T. E., Brotherton, M. S., Du, P., et al. 2024, ApJS, 272, 29
Zhang, Z.-X., Du, P., Smith, P. S., et al. 2019, ApJ, 876, 49
Zu, Y., Kochanek, C. S., Kozłowski, S., et al. 2013, ApJ, 765, 106
Zu, Y., Kochanek, C. S., & Peterson, B. M. 2011, ApJ, 735, 80